Small Molecule Detection by Surface Plasmon Resonance:

Improvements in Sensitivity and Kinetic Measurement

by

Christopher Assiff MacGriff

A Dissertation Presented in Partial Fulfillment
of the Requirements for the Degree
Doctor of Philosophy

Approved October 2013 by the
Graduate Supervisory Committee:

Nongjian Tao, Chair
Shaopeng Wang
Joshua LaBaer
Junseok Chae

ARIZONA STATE UNIVERSITY

December 2013

ABSTRACT

Surface plasmon resonance (SPR) has emerged as a popular technique for elucidating subtle signals from biological events in a label-free, high throughput environment. The efficacy of conventional SPR sensors, whose signals are mass-sensitive, diminishes rapidly with the size of the observed target molecules. The following work advances the current SPR sensor paradigm for the purpose of small molecule detection. The detection limits of two orthogonal components of SPR measurement are targeted: speed and sensitivity. In the context of this report, speed refers to the dynamic range of measured kinetic rate constants, while sensitivity refers to the target molecule mass limitation of conventional SPR measurement.

A simple device for high-speed microfluidic delivery of liquid samples to a sensor surface is presented to address the temporal limitations of conventional SPR measurement. The time scale of buffer/sample switching is on the order of milliseconds, thereby minimizing the opportunity for sample plug dispersion. The high rates of mass transport to and from the central microfluidic sensing region allow for SPR-based kinetic analysis of binding events with dissociation rate constants (k_d) up to 130 s^{-1}. The required sample volume is only 1 μL, allowing for minimal sample consumption during high-speed kinetic binding measurement.

Charge-based detection of small molecules is demonstrated by plasmonic-based electrochemical impedance microscopy (P-EIM). The dependence of surface plasmon resonance (SPR) on surface charge density is used to detect small molecules (60-120 Da) printed on a dextran-modified sensor surface. The SPR response to an applied ac potential is a function of the surface charge density. This optical signal is comprised of a dc and an ac component, and is measured with high spatial resolution. The amplitude and phase of local surface impedance is

provided by the ac component. The phase signal of the small molecules is a function of their charge status, which is manipulated by the pH of a solution. This technique is used to detect and distinguish small molecules based on their charge status, thereby circumventing the mass limitation (~100 Da) of conventional SPR measurement.

To my parents, who taught me how to do my best

ACKNOWLEDGEMENTS

I gratefully acknowledge the tutelage and support of my advisor Dr. NJ Tao. Dr. Tao has taught me how to be a more strategic problem-solver and communicator of complex scientific information. I would also like to thank my committee for their guidance and constructive criticisms; Dr. Shaopeng Wang deserves a special thank you for many helpful discussions. I benefitted tremendously from the expertise and helpfulness of Dr. Kyle Foley, Dr. Xiaonan Shan, and Dr. Wei Wang. I have had the privilege of working in an extraordinary research group and I am thankful for the experience.

TABLE OF CONTENTS

CHAPTER Page

CHAPTER Page

LIST OF TABLES

Table Page

LIST OF FIGURES

Figure Page

1. STATE OF THE ART

1.1 Introduction

The interactions between small molecules and biological macro-molecules constitute one of the most important components of biological networks. Communication between cells, expression of genes, and the entire immune system are dependent on a massively parallel network of binding interactions of proteins and small molecules. The development of drug candidates and the identification of biomarkers for clinical diagnosis rely on rigorous, quantitative measurements of binding events between small molecules and their biological receptors. Methods for elucidating these types of binding reactions are paramount for understanding of one the most fundamental mechanisms of biology.

The term 'small molecule' is ambiguous. In the context of this report, it refers to molecules with a molecular weight of less than 1000 g/mol (or Daltons). The average mass of a human protein is on the order of a few tens of kDa, but can be larger or smaller by several orders of magnitude [1]. Note that the small molecules defined above are on average an order of magnitude smaller than a typical human protein. Drugs and therapeutic agents are two examples of widely studied small molecules.

This chapter analyzes the current status of research and technology associated with the measurement of small molecule binding interactions with larger biomolecules. These biomolecules include, but are not limited to, peptides, enzymes, antibodies, DNA, RNA, and aptamers. The basic theory governing bi-molecular reactions is introduced. The type of binding interactions analyzed will be limited to non-covalent binding.

Chapter 2 introduces the theory of surface plasmons. The chapter progresses from a theoretical description of surface plasmon behavior (more in Appendix A) to methodologies for

their excitation. Chapter 3 presents the useful application of these phenomena in the form of SPR-based biosensors. The focus of chapter 3 is on the practical issues and optimization strategies relevant to the use of SPR in scientific research.

Chapter 4 introduces the four-port microfluidic cell and its use for high speed SPR kinetic measurement. The time resolution (as defined by the rate of sample delivery and removal) of this device is 100 times faster than any previously reported related technique.

The theory and application of Plasmonic-based Electrochemical Impedance Microscopy (P-EIM) is detailed in Chapter 5. P-EIM is used to detect the presence of molecules based on their charge. The presence of molecules with a molecular weight of 60 Da is detected by P-EIM, improving the lower mass detection limit of 95 Da as reported in the literature.

1.2 Bi-Molecular Reaction Kinetics

Before the specific mechanisms of various kinetic measurements are discussed, it is useful to consider what happens to signal 'central' molecule that takes part in a reaction. Following the methodology of Schilstra and Martin [2], species (*e.g.* small molecules, peptides, enzymes, *etc.*) will be indicated with capital letters (X, Y) and specific instances of a species (*e.g.* a small molecule, a peptide) with lower case (x, y). The number of instances or items of a particle species in an enclose compartment will be written as n subscripted with the species name ($n_{\mathrm{X}}, n_{\mathrm{Y}}$). Square brackets around the species name indicate concentration ($[X], [Y]$). The number of items expressed in moles per unit volume:

$$[X] = \frac{n_{\mathrm{X}}}{N_{\mathrm{A}} V} \tag{1}$$

Here V is the volume of the container and N_{A} is Avogadro's number, 6.023 x 10^{23} items per mole.

If the central molecule is a reactant of type X in the bimolecular reaction $X + Y \rightarrow Z$, the molecules must be able to find each other for the reaction to occur. The frequency with which type Y molecules collide with small molecule x is proportional to the concentration of Y. Additionally, the frequency is a function of the temperature and viscosity of the surrounding medium. Once the two molecules come into contact with each other, their respective orientations must be correct to result in a binding event. We will make an assumption (which may not always be valid) that the factors affecting the orientation and therefore the number of successful binding events is kept constant.

Now consider the bimolecular reaction between 1000 items of the same species as the central molecule. The probability that any one of these molecules with undergo a successful collision/reaction with a molecule from group Y is 1000 times greater, provided that the molecules do not hinder or inhibit each other. We may conclude that the rate at which the reactant molecules are consumed is proportional to the number of items in one species and the concentration of the other:

$$-\frac{dn_{\mathrm{X}}}{dt} = -\frac{dn_{\mathrm{Y}}}{dt} = k_1 \cdot n_{\mathrm{X}}[Y] = k_a \frac{n_{\mathrm{X}} n_{\mathrm{Y}}}{N_{\mathrm{A}} V} \tag{2}$$

The first two terms represent the rates at which X and Y items disappear from the medium, respectively. If time is measured in seconds, and volume in liters, the dimensions of the expressions are s^{-1} and the dimension of the proportionality factor k_1 is $M^{-1}s^{-1}$. Dividing both sides by $N_{\mathrm{A}}V$ gives the reaction rate expression in terms of concentrations:

$$-\frac{d[X]}{dt} = -\frac{d[Y]}{dt} = k_1 \cdot [X][Y] \tag{3}$$

Reactions of this form are known as second order reactions, with k as a second-order rate constant, because the total power to which the concentrations of all reactant species are raise is 2 ($[R_{\mathrm{X}}]^1 \cdot [R_{\mathrm{Y}}]^1 = [Reactants]^2$).

After the small molecule has spent some time bound with a member of species Y, it will either dissociate (in a reversible reaction) or remain bound indefinitely (in an irreversible reaction). The rate at which the complex Z dissociates is considered a first order reaction because it is a function of only concentration:

$$-\frac{dn_{\mathrm{Z}}}{dt} = k_2 n_{\mathrm{Z}} \Rightarrow -\frac{d[Z]}{dt} = k_2[Z] \tag{4}$$

The unit of the proportionality factor k_2, or first order rate constant, is s^{-1}. First-order reaction rates are independent of the volume of the compartment in which the reaction takes place.

1.3 Measurement Techniques

Traditionally, it has been difficult to measure the binding affinities of small molecules. For most transducers, the signal is proportional to either the mass or concentration of the reactants. The diminutive size of small molecules presents an immediate obstacle in their detection. Many biologically relevant small molecules are only available at low concentrations, further exacerbating the difficulties associated with small signal detection. Several techniques that were previously limited to measurements in the domain of large-scale targets have been improved to measure small molecules, for example, Mass Spectrometry and Enzyme-Linked Immunoassays. Other techniques such as Fluorescence Correlation Spectroscopy and Förster Resonance Energy Transfer have been developed to address limitations in sensitivity of other

techniques. Emerging nanotechnologies like quantum dots and nanowires demonstrate novel but still immature small molecule affinity assays. Among the techniques discussed, Isothermal Titration Calorimetry and Surface Plasmon Resonance represent two of the most information-rich measurement techniques, particularly with respect to thermodynamic and kinetic information.

1.3.1 Mass Spectrometry

The vast field of mass spectrometry (MS) is widely used to study the non-covalent complexes formed between small molecules and biomolecules. The variety of techniques, and most notably, the combination of chromatography and mass spectrometry, promotes a varied and flexible approach to studying bimolecular interactions. Affinity techniques employing MS identify compounds based on the ratio of mass to charge and provide a label-free method of characterizing new chemical entities that interact with the target biomolecule [3]. Mass spectrometry-based methods may directly or indirectly characterize bound complexes formed between small molecules and their receptors.

Mass spectrometry is used to identify the binding components by measuring the mass to charge ratio of the sample. Bound complexes formed (preferably) in solution are treated such that they enter the gas phase with bound excess charge(s). A mass analyzer then sorts the ions with electromagnetic fields according to their mass. Ions passing by or hitting the detector surface either induce or charge or generate a current, respectively. The number of ions involved in measurements is sufficiently small that the signal is often amplified by an electron multiplier.

Under appropriate experimental conditions, MS is used to directly analyze the complexes formed under native conditions. The three primary methods to determine the affinity

constant K_D in gas-phase measurements that reflect those in solution are (1) raising the temperature of the analyte solution and using MS to determine the percentage of intact complexes [4-5], (2) competition-based experiments to measure the stability of the bound complex [6, 7] and (3) titration of a small molecule with its binding partner [8, 9]. It is important not to disrupt the non-covalently bound complexes and to ensure the mass spectra accurately represents the solution-phase chemistry. Electrospray ionization [10] (ESI) MS and matrix-assisted laser desorption/ionization [11, 12] (MALDI) MS are the two most commonly used direct characterization methods.

Most MALDI applications rely on solid organic matrices for the ionization of the sample [13]. These crystalline matrices are often responsible for significant background noise and may complicate analysis of low molecular weight compounds [14]. Therefore careful sample preparation and design of experiment is necessary. MALDI-MS has consistently demonstrated reliable measurement of small molecules from 100 Da to 1.5 million Da [13].

Electrospray ionization MS methods are widely used to characterize the affinities of small molecules to biomolecules [15]. In addition to direct detection of solution-phase complexes, ESI-MS can be combined with ion activation techniques such as tandem MS, to probe the composition and topology of the complexes [16, 17]. Despite the widespread use of ESI-MS, the mass spectra may not accurately reflect solution composition of the complex and false positives from non-specific adsorption between solution components are difficult to remove [18]. That being said, many researchers have pursued rigorous, repeatable experiments utilizing the soft-ionization technique of ESI to measure small molecule interactions with great success.

In contrast to direct measurement, indirect methods must prepare and separate the complexes prior to analysis by biochemical and chromatographic methods. In this methodology, mass spectrometry is used to identify and characterize the small molecules independently of their binding partner. The bound complexes are often exposed to denaturing solutions to induce dissociation. This method measures the molar ratio (average loading) of the two components and not the binding stoichiometry (distribution) between the two [19].

There are numerous reports of affinity-based assay formats that have been directly coupled with MS, creating highly sensitive and specialized detection platforms. Affinity-selection [20], pulsed-ultrafiltration [21] (PUF-MS), and frontal affinity chromatography [22] (FAC-MS) have proven successful in identifying novel small molecule/receptor interactions. A number of examples are presented in Table 1.

Table 1. MS-based methods for use in small molecule/receptor detection

Method	Target	Potential Receptors	Principle
Frontal-affinity chromatography-MS	Immobilized in a column	Pumped through column	Compounds in dynamic equilibrium with immobilized target. Unbound and weakly bound compounds elute earlier than bound. Mass-specific detection identifies compounds
Pulse ultrafiltration-MS	Mixed with multiple compounds in solution	Mixed with target in solution	Target mixed with potential ligands is placed over ultrafiltration membrane; when pressure is applied, ligands showing affinity for the protein are selectively concentrated; later, they are identified by MS
Affinity size exclusion-MS	Mixed with multiple compound in solution	Mixed with target in solution	Rapid molecular exclusion fractionation is a spin column separates target-ligand complexes from unbound compounds; MS identifies binders
Ultrafiltration-MS	Mixed with multiple compounds in solution	Mixed with target in solution	Target mixed with ligands and subjected to centrifugal ultrafiltration; binding compounds separated from non-binders are washed to waste; ligands bound to target are eluted by acidification and detected by MS
Affinity capillary electrophoresis-MS	In electrophoretic buffer	In running buffer for CE	Changes in mobility upon binding indicate bound ligands in electrophoretic buffer; MS identifies the binding partner
Surface plasmon resonance-MS	Coupled to optical surface	Flow across sensor surface	Changes in surface refractive index indicate presence of binding partner for an immobilized target; MS identifies the binding partner
Affinity capture-MS	Immobilized on beads	Incubated with immobilized target	Bead-bound target mixes with potential ligands; unbound ligands removed by washing; bound ligands eluted and identified by ES-MS/MS
Noncovalent affinity	In gas phase	Mixed with one or multiple targets	Direct mass-analysis of target-ligand mixture, complex of a ligand with one or multiple targets is identified directly from its mass using very soft ionization from volatile buffer

Independent of the different hardware configurations, all affinity selection-mass spectrometry (AS-MS) based platforms follow a basic experimental procedure which includes the following steps [23]: (1) the small molecule is mixed with a pool of potential ligands, (2) the resultant small molecule/receptor complex is separated from the non-binding mixture components, and (3) the receptors specific to the small molecule query are identified by MS. Bound components are characterized by their molecule weights or collision-induced fragmentation patterns and are directly identified, thereby decreasing the number of false positive binding receptors and reducing non-specific adsorption [24]. Depending on the specific platform, the small molecule/receptor can either be viewed directly in the spectrometer or detected as a perturbation or abnormality in the unbound receptor behavior. The latter detection method is considered more biologically relevant. MS direct detection is done in the gas phase, while the secondary measurement is often measured as elution from a column, which is done in the liquid phase.

Pulsed ultrafiltration-mass spectrometry (PUF-MS) has been developed for the selection, identification, and characterization of low molecular-weight compounds that interact with enzymes, proteins, and other macromolecules. This technique utilizes the disparity of size between the unbound small molecules and the bound small molecule/receptor complex. A macromolecular receptor is immobilized in the ultrafiltration cell, which is made of a material that impedes non-specific adsorption of the small molecule analytes (*e.g.* PEEK). The analytes flow into the cell and selectively bind to the immobilized receptor. An ultrafiltration membrane is chosen such that it is only permeable to unbound small molecules. Bound ligands are eluted from the chamber by destabilizing the small molecule/receptor complex with an organic solvent

or pH change. The eluate (small molecules) is then analyzed by either on-line MS or characterized by a High Performance Liquid Chromatography column, and analyzed with LC-MS or tandem LC-MS/MS [25]. As the small molecule alternatively associates and dissociates from the receptor, its elution from the cell is slowed (relative to a control cell without immobilized receptors). From this measurement, the affinity of the small molecules for the immobilized receptor can be quantitatively measured [26].

The frontal affinity chromatography method extracts binding constants from the effect of small molecule concentration on the frontal retention time [27]. Similar to PUF-MS, the receptor is immobilized in a column and a mixture of small molecules is pumped through the column. A mass spectrometer is attached in series to the column and measures the concentration of small molecules passing as they elute. Compounds that have an affinity to the receptor will experience a delay in elution related to how long (*i.e.* how strongly) they bind to the immobilized receptor. This method, first developed by Kasai et al. [28], differentiates itself from PUF-MS by its ability to detect binding events in a concentration independent fashion. It is possible to detect binding events at concentrations well below their K_D values [29]. Additionally, this method is equally viable for measuring both soluble and membrane-bound receptors. The column can be prepared and reused with very low capacities (less than 2 pmol of binding sites) and can measure low K_D values (~ 2 nM) [30].

Proponents of affinity capillary electrophoresis laud the technique's speed of assay, minimal sample volume required, free solution-based measurements, and low cost. Normal sample consumption is on the order of a few nanoliters, and minimum sample volume is a few tens of microliters, making ACE-MS competitive with techniques such as gel filtration

chromatography, dialysis, classical gel electrophoresis, calorimetry, and surface plasmon resonance [31]. The receptor is exposed to potential binding candidates and changes in its electrophoretic mobility are used to determine the affinity of the receptor/small molecule binding event. The amount of free and bound receptors (or small molecule) need not be known [32]. Using laser-induced fluorescence, binding interactions of labeled target or ligand can be detected at very low concentrations (nM to pM) [33].

The simplicity of rapid size-exclusion chromatography coupled with MS (SEC-MS) is appealing; the receptor is neither trapped nor immobilized, and the small molecule/receptor complex is separated from unbound small molecules on the basis of size. As the unbound receptors and small molecules are excluded, the bound receptor/small molecules are no longer in equilibrium. The bound complex will begin to dissociate immediately, so speed in analysis is imperative in this type of measurement [34]. SEC-MS [35], along with FAC-MS [36], are capable of achieving high-throughput assay measurements by screen thousands of compounds in the same assay and identifying active compounds by using mass-selectivity. Successful high-throughput screening can help narrow the focus from millions of possible interacting pairs to tens or hundreds.

Mass spectrometry is a very powerful tool used for the characterization of small molecule binding. The mass resolution of MS is unparalleled; modern instruments can easily distinguish ions differing by only a single atomic mass unit. There are many different MS instrument configurations, which is indicative of its usefulness and versatility. Kinetic measurements with MS are currently limited to measuring the equilibrium binding affinity K_D.

1.3.2 Enzyme-Linked Immunosorbent Assay

The enzyme immunoassay [37] (EIA) and enzyme-linked immunosorbent assay [38] (ELISA) were simultaneously developed independently of each other in 1971, with both techniques based on the principles of immunoassays with an enzyme as the reporter label. Their forerunner, radioimmunoassay [39] (RIA) was developed by Berson and Yallow a decade earlier; Yallow was later awarded the Nobel Prize for Medicine for the technique. The impact this technology has had is incredible in scope; there have been more than 100,000 research articles published that are related to these three techniques.

In a typical ELISA assay, an analyte is immobilized to a primary biomolecule immobilized in a well on a polystyrene plate. The secondary biomolecule, linked with an enzyme, is then attached to the bound complex. Unbound material is then easily washed away. Enzyme-related activity is then measured after incubation with an enzyme substrate. The most commonly used enzymes are horseradish peroxidase and alkaline phosphatase. The choice of substrate depends on the desired sensitivity and signal detection instrumentation (fluorometer, spectrophotometer, *etc.*).

Immunoassays rely on either competitive or immunometric detection. The goal of immunoassays is to measure a specific binding reaction. Therefore a signal must be generated that reflects the extent of the binding. Competitive-binding assays (CBA) produce a signal that is proportional to the number of unbound target biomolecules. Immunometric assays, on the other hand, measure the amount of bound analyte/biomolecule complex.

In competitive-binding assays, a label is usually placed on the analyte to be measured. As described by Bock [40], a fixed concentration of labeled analyte reagent and a fixed (and

comparably low) concentration of the biomolecule reagent are combined with the variable concentration of unlabeled analyte in the sample. As the concentration of unlabeled analyte in the sample increases, the amount of label that will bind to the biomolecule decreases. The original RIA was a CBA using insulin labeled with the gamma-emitter diode [39]. There are numerous types of labels employed today to measure small molecule binding events. The presence of a label is another primary classification of immunoassays.

ELISA has emerged as a common immunoassay, and it's most common variation, the sandwich assay, demonstrates clearly the principles of the immunometric assay. In a sandwich assay, the analyte to be detected is sandwiched between its primary target (biomolecule) and its presence is detected by secondary biomolecule, which could be radio labeled (RIA) or linked to an enzyme (ELISA), which is used to report the analyte's presence. The analyte to be detected must be free to bind to two receptors: its primary target and a secondary label. The simultaneous binding of two biomolecules to the analyte is an extremely specific process. That is, the possibility of non-specific interactions is lowered by requiring the analyte to bind to two partners. Additionally, because signaling is often coupled to a catalytic (enzymatic) signaling mechanism, ELISA can routinely detect sub-nanomolar [41] targets, and has demonstrated utility in the picomolar [42] concentration range. The measured equilibrium dissociation constant K_D between the analyte and primary target can be estimated by the strength of the secondary label's signal.

Direct detection in ELISA is not widely used. This method uses a labeled primary target that interacts directly with the analyte. The analyte or target biomolecule may be immobilized on the sensor surface. Labeling the primary target can significantly alter its binding affinity,

especially if the label is as large as an enzyme. Additionally, this method has limited signal amplification.

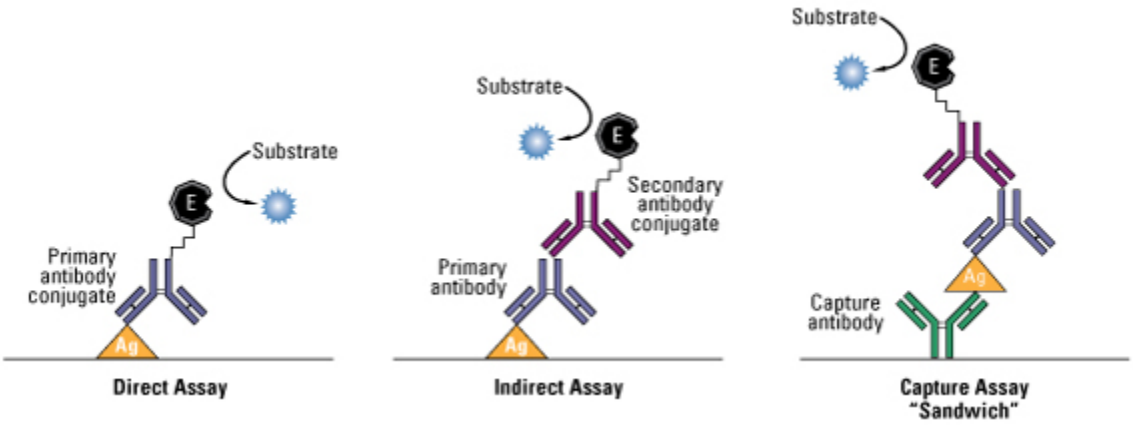

Figure 1. ELISA formats. The antigen (*e.g.* small molecule) of interest is immobilized to the assay plate or an immobilized antibody (*e.g.* receptor). Detection of the antibody is performed either directly or indirectly. [From Thermo Scientific at http://www.piercenet.com]

There are several obstacles for ELISA-based small molecule affinity analysis. First, ELISA is a single analyte detection method. During a typical ELISA assays, one type of protein is detected per well. Second, the analyte concentration range is limited to approximately two orders of magnitude, limited by the signal to noise ratio and tendency of the fluorophores to photobleach. Finally, the requirement of two biomolecules to the analyte is nontrivial. Small molecules may be unable to simultaneously bind to more than one biomolecule due to steric hindrances. On the other hand, many proteins can bind two or more antibodies at a time. For this reason, ELISA is primarily used to measure proteins binding to a primary antibody, which is detected by the subsequent binding of a fluorophore-labeled secondary antibody.

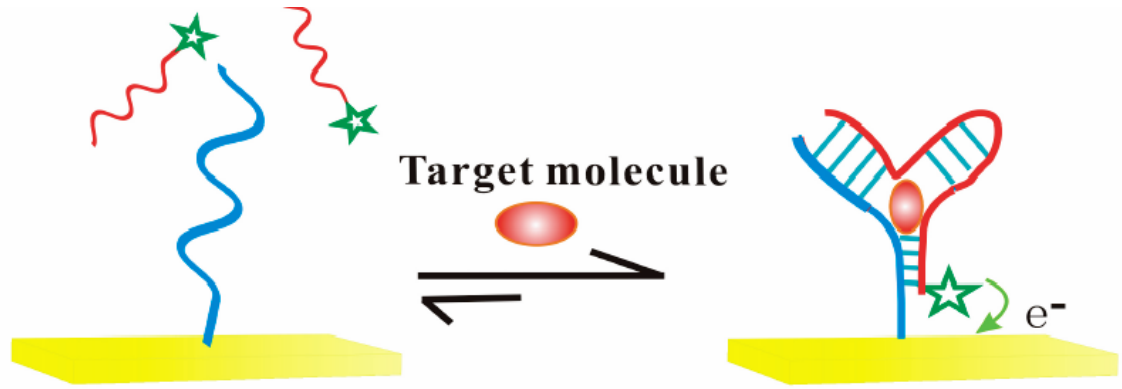

Figure 2. Novel electrochemical sandwich array based on small molecule binding to a split aptamer; binding is confirmed by a change in faradaic current. From reference [43].

While ELISA in its original form may be poorly suited for direct detection of low molecular weight small molecules, the sandwich assay principle has inspired novel detection platforms. One such technique uses short DNA or RNA sequences, called aptamers [44, 45], to specifically bind small molecule targets. A single aptamers, split into two fragments, will tend to bind to stay dissociated. If the aptamer binds the small molecule with high affinity, the presence of the small molecule will drive the equilibrium towards the association of the intact aptamers/small molecule complex. Fabrication of the novel sequences is relatively easy and they demonstrate a wide range of selectivity and affinities [46]. In principle, aptamers are superior to antibodies for use in bioanalysis; aptamers demonstrate superior stability against biodegradation and denaturation in addition to providing a useful response against non-immunogenic molecules. However, since their introduction 20 years ago, the number of targets for which multiple, distinct aptamers have been fabricated is small [47].

1.3.3 Nanomaterials

Nanomaterial-based protein and small molecule biodiagnostic screening has demonstrated excellent potential as an assay format. Nanoscale detection systems have significant advantages over traditional assay formats with regards to sensitivity and selectivity. Many of the same techniques used for novel, nanoscale detection of the presence (diagnostic screening) of small molecules can be used to determine their stoichiometry (binding affinities) as well. However, this technology is not nearly as well established as MS or ELISA, and is not yet ready for widespread use. Much of the research in this field is still in the 'proof of concept' stage and requires significant optimization and critical analysis before it enjoys mainstream success. The eagerness to measure events on the nanoscale is evidenced by the variety of detection methods that have been reported in the last 20 years. The sensitivity of nanomaterial-based assays has inspired many novel detection systems.

Protein and small molecule nanomaterial-based assays are primarily divided into two major categories: optical detection of nanoparticles (NP) and electrical detection with nanowires (NW) or nanotubes. The optical signal from NPs can be altered by specific interactions between nanoparticle-bound biomolecules and small molecule targets. The same type of interactions can generate an electrical signal in NWs.

For the last two decades, the gold standard in the field of protein diagnostics has been ELISA, which relies upon fluorophore labeling [48]. ELISA is a robust, sensitive (~pM detection limit) technique that is relatively easy and cheap to implement in a laboratory or clinical setting. Nanomaterial-based assays must compete directly with the limitations of ELISA to be considered a viable assay format. The molecular fluorophores employed in ELISA suffer

from shortcomings such as photobleaching, broad absorption and emission characteristics, and relatively expensive equipment to detect their presence in an assay. The physical properties of nanoparticles are more flexible than those of molecular fluorophores; the specific emissive, absorptive, and light-scattering properties of metallic nanoparticles and quantum dots can be systematically varied base upon their fabrication method [49-51]. Nanowires and nanotubes can be tailored in an analogous manner; their specific composition can be controlled to produce measurable changes in conductance in response to small molecule binding [52].

1.3.3a Nanowires

Nanowire-based sensors are designed to either measure changes in conductance between two contacts or as field-effect transistors (FETs). In the first variation, the adsorption of small molecules onto the surface of a nanowire can cause a significant change in the wire's resistance. On a large scale, the resistance of a metallic wire is dominated by lattice scattering and is mostly insensitive to chemisorption. When the scale of the wire reduces to the nanometer scale of the mean free path of the electrons, the conductance mechanism becomes ballistic and is sensitive to changes in the conduction electron density its surface. The conductance change in a NW is proportional to the strength of the binding between the wire and the small molecule. Nanowires used as conductometric sensors have successfully been used to measure the presence and of test gases [53]. In the FET-based measurements, the binding of biomolecules changes the threshold voltage and generates measurable changes in the conductance of the device. FET-based sensors have demonstrated direct, label-free, real time measurements of small molecule [54] and protein binding [52, 55].

In the NW FET, the threshold voltage, which creates a conducting path between a source and drain, is modified by the addition of biomolecules on a gate electrode. The laboratory of Lieber [56] has published several experiments demonstrating the utility of this detection principle on the nano-scale. Small molecule binding to biomolecules has already been reported: the dissociation constant of ATP binding to Abl kinase and kinetic information of its small molecule-inhibitors were directly measured [57] by monitoring real-time changes in device conductance.

The advantage of nanoscale detection introduces an interesting new set of experimental considerations, some of which we do not yet fully understand. The most notorious of which is the discrepancy between the theoretical and reported detection times. Theoretically, the time scale of diffusive transport of sub-picomolar concentrations in nanoscale sensors requires binding measurements to last hours or days [58]. More sophisticated convection-reaction-diffusion theory predicts that binding events will last for tens of minutes, but to be spaced several days apart [59]. However, femtomolar detection levels are common in nanowire experiments (Lieber and Stern independently) and the reported measurement times last only a few minutes. This disparity suggests there must either be something accelerating the binding or our understanding of the physics of this small scale is still incomplete. Kinetic information extrapolated from nanowires must therefore be examined critically. The small quantity of molecules used, the sensitivity, and the possibility of making very large integrated arrays make nanowire-based kinetic measurements potentially very useful.

1.3.3b Nanoparticles

For quantitative biosensing, such as affinity measurements, nanoparticles are conjugated with small molecule- (or more usually peptide-) specific recognition molecules (biomolecules) such as antibodies, DNA probe molecules, biotin/streptavidin, or enzymes. The success of fluorescence-based spectrometry for protein and gene detection today can be accredited to five fundamental attributes [60]: (1) each label can potentially provide 107-108 photons per second which allows for fast signal acquisition; (2) multicolor dyes can be used for multiplexed assays; (3) single molecule detection is a common focus of current research, demonstrating high sensitivity; (4) the luminescent signal is localized (unlike some enzyme-linked amplification schemes; (5) the labeling process can be straightforward provided that functional groups are available on the label target. Three major detection approaches are Fluorescence Correlation Spectroscopy (FCS), Fluorescence (or Förster) Resonance Energy Transfer (FRET), and Localized Surface Plasmon Resonance (LSPR). All three techniques can measure binding affinities.

Fluorescent Correlation Spectroscopy measures fluctuations in photon count rate as low concentrations of molecules and/or complexes (~nM) diffuse through an extremely small observation volume (~fL). Confocal microscopy and two-photon optical techniques are most often used to define small observation volumes and avalanche photodiode detectors measure the intensity fluctuations of the fluorescent signal [61]. There are several fluorescent labeling strategies, but all rely on a change in signal as a result of a change in the diffusion (*i.e.* mass) of the bi-molecular complex. A molecule labeled with a molecule fluorophore or nanoparticle has a characteristic diffusion through a particular medium under standard conditions. If the small

molecule binds to a large biomolecule, such as a peptide or enzyme, the diffusion time through the detection volume will change. FCS is one of the few techniques that can directly measure binding rate constants (*e.g.* $k_d[\mathrm{s}^{-1}]$), not just the affinity (K_D[M]) of bi-molecular interactions.

The effect of labeling on the diffusion of the targets can be problematic in FCS. The addition of a small molecule may not change the diffusion of a massive binding partner. There have been very few FCS reports of small molecule binding events due to the difficulties associated with labeling small molecules. Molecular fluorophores and small molecules have comparable molecular weights (~100s of Da). It is obvious that characteristic diffusion of a small molecule would be compromised upon labeling. It is also reasonable to assume that such a label will affect its binding characteristics. The limitation that biomolecules are labeled in standard FCS measurements is currently being addressed by Inverse-FCS and Inverse Cross-correlation FCS, which instead labels the surrounding medium with fluorophores and measures the transient dips in signal intensity due to displacement of the medium by diffusion small molecules/complexes [62]. For the time being, FCS measurements are generally not useful for small molecule kinetic studies.

Many Förster resonance energy transfer (FRET) assays for protein quantification have been developed for use with gold nanoparticles (AuNP) and quantum dots (QD). In a basic FRET measurement, a donor molecule is excited by radiative energy of a particular wavelength, which it then transfers (typically over long distances of 1-10 nm) to an acceptor molecule. The acceptor molecular may then quench the signal from the donor molecule or re-emit the radiative energy at a longer wavelength. Ideally, the fluorescence of the acceptor molecule (in Fluorescence-RET) is contingent upon a donor molecule nonradiatively donating its energy. In

reality, direct acceptor excitation, photobleaching, and spectral crosstalk can lead to misleading or false signals. The use of gold nanoparticles and quantum dots has helped to mitigate these effects and have successfully been used in the measurement of small molecule binding affinities.

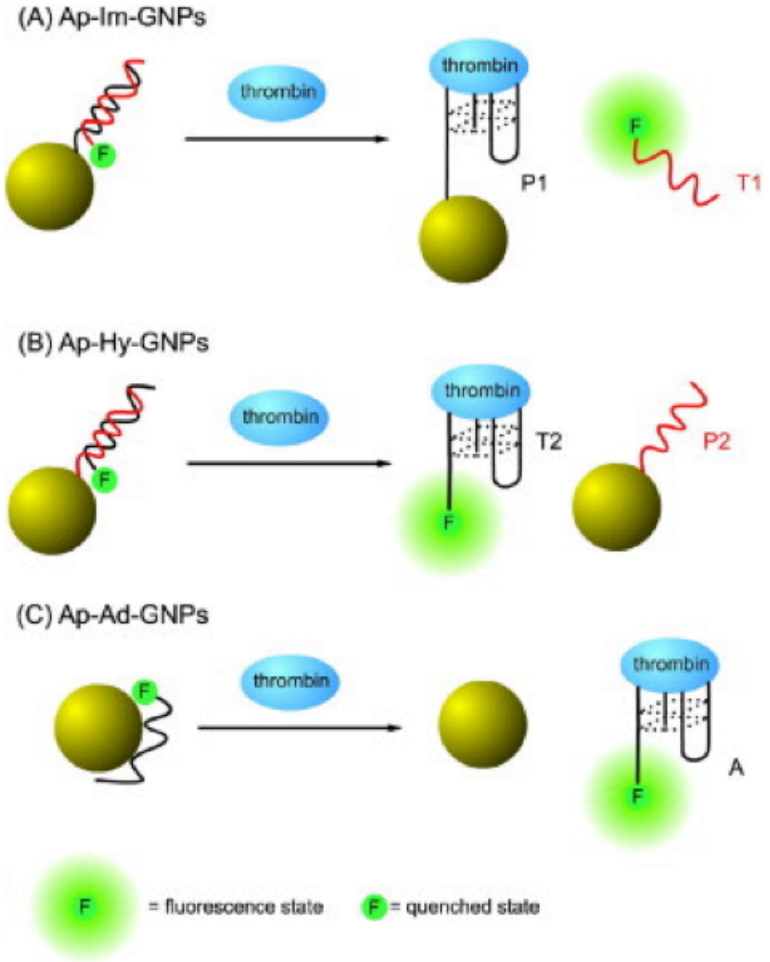

Figure 3. AuNP-FRET experiment methodology. From reference [64].

Gold nanoparticles are most often employed as acceptor materials in FRET-based biosensors due to their high molar extinction coefficient [63]. Wang et al. [64] used AuNPs linked to an aptamer to quench fluorescence from a dyed DNA label. In the presence of thrombin protein, the dyed single-strand DNA (ssDNA) dissociated in manner proportional to

the affinity of the protein to the aptamer/gold nanoparticle target. The kinetic affinity was determined by the amount of unquenched fluorescence from the displaced DNA label.

Several variations of this experimental setup were investigated in the same paper. In the second approach, the AuNP were linked to the ssDNA, and the aptamer target was labeled with the donor molecule. The quenched AuNP/ssDNA/aptamer complex dissociated in the presence of thrombin and the measured fluorescence was used to directly detect the presence of bound aptamer/thrombin. Finally, the aptamer linked to the AuNP and was once again labeled. The binding of thrombin induced a change in conformation in the aptamer, releasing it from the AuNP, and the fluorescence was unquenched. The three difference labeling techniques generated three different kinetic affinities, demonstrating the non-trivial impact of labeling on kinetics.

Quantum dots are commonly used as donor molecules in FRET-based assays [65, 66]. The emission wavelength of quantum dots is tunable via controlling the particle diameter size. QDs have a large Stokes shift, so that the difference in absorption and emission wavelength is very large. Using QDs as donor molecules in a FRET experiment, Medintz et al. [68] quantified the binding affinity of small molecule maltose to maltose binding protein (MBP), which was attached to QDs. The fluorescence of the QDs was initially extinguished by attaching the quencher QSY9 to the MBP/QD complex. The addition of maltose competed for binding sites with the quencher and the amount of bound maltose with the MBP/QD was quantified by the resulting fluorescence of the bound complexes.

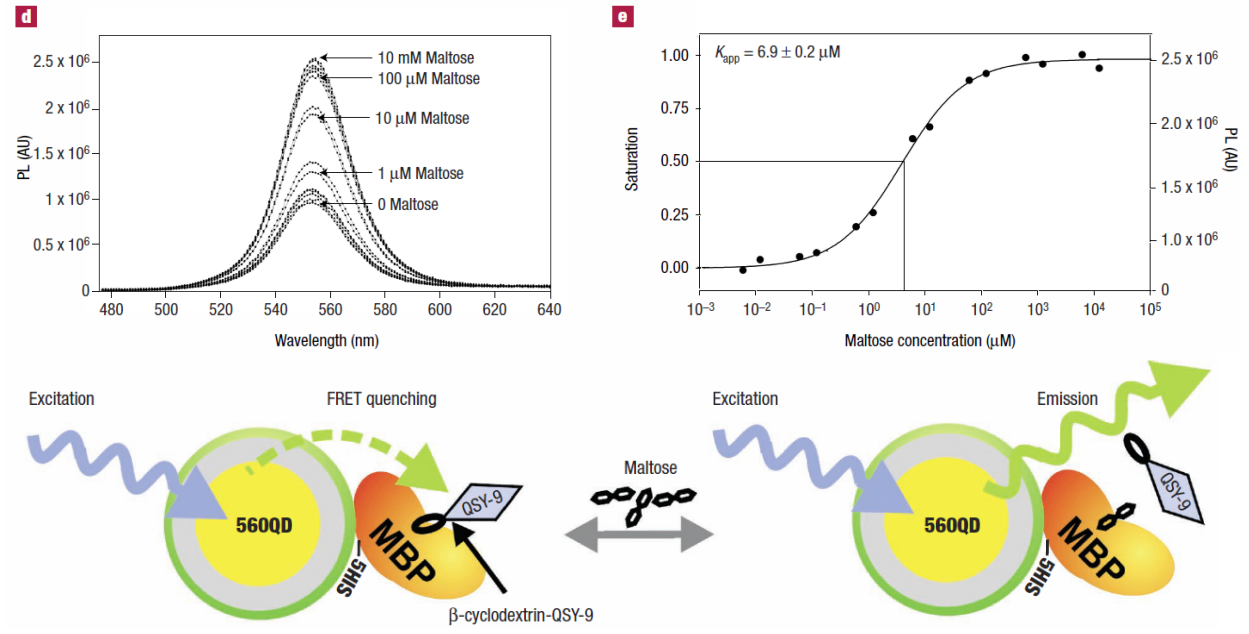

Figure 4. Determination of the dissociation equilibrium constant using quantum dots. From reference [68]

In general, there are two strategies to achieve high sensitivity: target-based amplification and signal-based amplification. In target-based amplification (*e.g.* Polymerase chain reaction) a generation of more targets or target surrogates is elicited by a recognition event. Current PCR techniques can reliably detect the presence of only a few copies of a nucleic acid sequence [67]. Conversely, in signal-based amplification a catalytic entity is often used to increase the indicator from a single binding event [68]. Mirkin et al. developed a method for signal-based amplification of small molecule binding to IgG1 and IgE based on the aggregation of AuNPs [69]. Small molecules biotin and dinitrophenyl (DNP) were tagged with oligonucleotides that were complementary to oligonucleotides coating the surface of the AuNPs, creating a nanoparticle complex that had an affinity for a target biomolecule (either IgG1 or IgE). When

the proteins were introduced to the small molecule/AuNP complexes, the aggregation of complexes induces a colorimetric change and the melting signature of the aggregates identifies which of the two proteins had bound. This technique is limited only to detecting the presence of a bound complex (and for all practical purposes, an irreversible binding) but demonstrates the potential for measuring very small quantities of the target molecules. Mirkin is credited with developing a bio-barcode assay (BCA) based on the amplification of an AuNP signal that has demonstrated zeptomolar sensitivity [70] to DNA binding and attomolar sensitivity to protein binding [71]. This approach may be applicable to measuring small molecule binding in the future.

Plasmonic nanosensors combine the localized sensitivity of nanoparticles with the established technique of surface plasmon resonance; the most common configuration relies on optical changes in thin gold films [72]. In this design, a localized electromagnetic field is created on the sensor surface, which resonates with the free electrons of the nanoparticles, resulting in an extremely intense and highly confined electromagnetic field. For example, a single 80 nm silver nanosphere scatters 445 nm light with a scattering cross section of 3×10^{-2} μm^2, a million times greater than the fluorescence cross section of a fluorescein molecule [73]. Plasmonic nanoparticles are generally 500,000 times more luminous than fluorophores [74].

There are two types of sensors based on the localized SPR (LSPR): aggregation sensors and refractive index sensors. The first sensor type relies on the drastic color change from NP aggregation due to near-field electromagnetic coupling; the resonance peak of two NP's red shifts as the distance between the two particles decreased below the particle diameter. If two NP were functionalized with complementary biomolecules, the interaction between the molecules

will induce the aggregation of the NP, which can be detected by the color change. The second sensor type relies on change in the local refractive index around the metal nanostructures. The size and shape of NPs can be varied to optimize the signal for a particular experiment, as their characteristic properties are a function of their geometry and composition.

Optical spectroscopy is currently the simplest method to detect LSPR on metal nanostructures. Extinction measurements are used to characterize large number of nanostructures such as nanoparticle colloids. Scattering measurements are used for low density nanostructures, often characterizing single nano-objects as single nanoparticles are visible using dark field microscopy. Extinction spectroscopy measurements tend to have a higher signal-to-noise ratio [75] but the spectroscopy approach is chosen based on the specific measurement to take place.

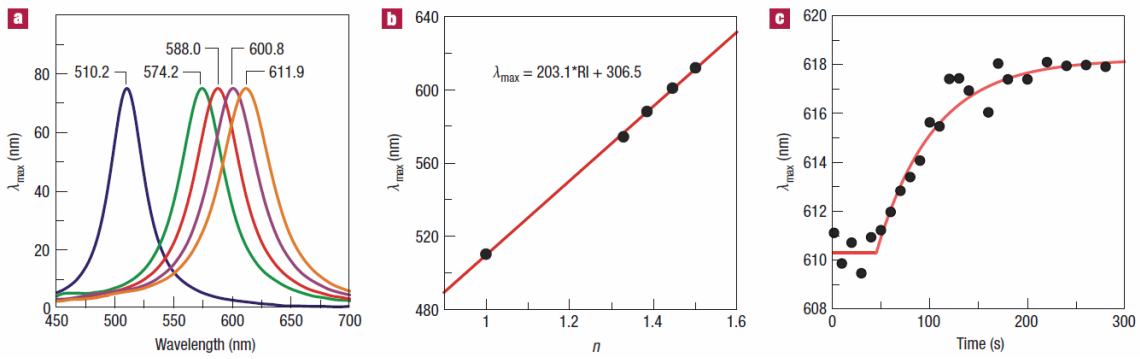

Figure 5. Representative data from a LSPR kinetic experiment. From reference [75]

Proof of principle experiments using localized SPR (LSPR) have been demonstrated for a variety of nano-structures, including triangular silver particles [76], gold nanodisks [75], nanoshells [77], nanorings [78], nanocrescents [79], and nanoholes [80] in thin films. Aggregation-based assays focus on the detection of low concentrations of target biomolecules

(*e.g.* small molecules [81, 82] , proteins [83, 84] and enzymes [85]) rather than real-time kinetic measurements. The binding stoichiometry K_D can be measured in the former, but not to a high degree of accuracy. Biosensing based on refractive index LSPR shifts are more suitable to kinetic rate (k_d) measurements, as their similarity to traditional film-based SPR measurements ensures their compatibility with established microfluidic platforms and assay protocols.

Small molecule affinity measurements based on localized changes in the refractive surrounding nanoparticles has been demonstrated as a proof-of-principle [86, 87]. The IC_{50} value, or the concentration that inhibits the curve by 50% from when no analyte is present, was determined at nanomolar concentration levels of stanozolol (a commonly abused anabolic agent with a molecular weight of 328 Da). Nanoparticle colloids were immobilized on a glass surface and were monitored via dark field spectroscopy. As the sensitivity of the system is dependent on the geometry and composition of the nanostructures, nanorods have been used to measure antibody/protein binding at picomolar concentrations.

The field of Raman spectroscopy has enjoyed an unexpected boon from the LSPR modes of nanoparticles in the form of a significant increase in sensitivity. The net electric field E_{net} around a dielectric particle is a combination of the applied field E_0 and the induced dipole field from the particle. For a polarizable spherical particle with a radius r_m and a dielectric constant ε_1, in a medium ε, the field gain G for the particle is [88]:

$$G(\omega) = \frac{E_{net}(\omega)}{E_0(\omega)} \approx 1 + \frac{\varepsilon(\omega) - \varepsilon_1}{\varepsilon(\omega) + 2\varepsilon_1}\left(\frac{r_m}{r + r_m}\right)^3 \tag{5}$$

Traditionally, the intense elastic scattering of Rayleigh light dominates the weaklier inelastic Raman scattering. Complex and expensive detection platforms are used to mitigate this

disparity. With the addition of metallic nanoparticles, both the excitation and the scattered fields of Raman spectroscopy are enhanced; surface enhanced Raman spectroscopy (SERS) routinely report signals 10^{12}-10^{14} times greater than signals from non-surface-enhanced experiments [89]. Small molecule [90] interactions and protein microarrays [91] have been reported with femtomolar concentration levels, although single molecule detection has been demonstrated by SERS [92, 93]. It is worthwhile to pursue such high levels of sensitivity. However, this technology requires substantial optimization and characterization before it can be routinely used to determine small molecule affinities.

Proponents of the nano-variety of SPR argue that it enjoys a simple detection setup and a reduced cost of analysis. The 'simplification' of this technique refers only to the lack of prism, which is necessary in the ubiquitous Kretschmann configuration in conventional SPR. The so-called reduced cost anticipates a dramatic decrease in the current fabrication expense, as it is still significant compared to evaporating or sputtering thin metal films. Furthermore, the instability of metal nanostructures towards changes in environmental conditions is still being addressed to provide more reliable and robust surfaces for LSPR measurements [94].

There are three major obstacles barring the widespread acceptance and adoption of nanoparticle-based assays [95]. The first concerns the reproducibility of nanoparticle production. Many properties of a nanoparticle depend directly on their size. Consistency and uniformity of nanoparticle size is mandatory for quantitative analysis of small molecule/biomolecule interactions. Second, the number of biomolecules attached per nanoparticle cannot yet be controlled. Multiple biomolecules can usually be attached to an individual nanoparticle. This ambiguity allows too much uncertainty for rigorous quantitative

kinetic measurement. Finally, and perhaps most importantly, biomolecules have demonstrated loss of activity upon conjugation to nanoparticles. This is a major point of contention in the debate between label and label-free bioanalysis. Even the smallest 2 nanometer ZnS nanoparticle has a mass on the order of tens of kilodaltons. Labeling a small molecule target biomolecule effectively doubles the mass, to say nothing of the molecular interaction forces, of the complex being measured. Even if the smallest label can be attached to the target biomolecule, the toxicity and biocompatibility of quantum dot labels is a source of the current controversy surrounding this technique.

1.3.4 Isothermal Titration Calorimetry

Isothermal Titration Calorimetry (ITC) is a powerful tool for characterizing small molecule binding events. ITC experiments provide a unique probe of thermodynamic information that can be used to quantify the binding stoichiometry, affinity, and enthalpy/entropy change. In other words, the information from ITC experiments can measure not only the magnitude of a binding, but which fundamental forces drive the interaction. ITC does not require the labeling of either binding partner, and the measurements are done exclusively in solution.

Isothermal titration calorimeters are first and foremost thermodynamic instruments designed to measure enthalpy changes in physical or chemical reactions. ITC employs thermocoupled sample and reference cells that routinely measure nanojoule heats of reaction [96]. The sample cell contains a biomolecular target for a small molecule. The small molecule is injected into the sample chamber at different concentrations, and the heat generated or absorbed during the binding is monitored. This corresponds to the change in enthalpy (ΔH) for

the interaction. The enthalpy change of a reaction can be determined one of two ways; it can be directly measured using calorimetry or indirectly by the van't Hoff method. Differential scanning calorimetry (DSC) and ITC are currently the only methods that directly measure ΔH [97]. The amount of heat evolved on addition of a small molecule to its binding partner in a 1:1 binding stoichiometry is:

$$Q = \frac{V_0 \Delta H [M]_t K_a [L]}{(1 + K_a [L])} \tag{6}$$

where V_0 is the volume of the cell, ΔH is the enthalpy of binding per mole of ligand, $[M]_t$ is the total macromolar concentration including bound and free fractions, K_a is the binding constant, and $[L]$ is the free ligand (small molecule) concentration [98]. The direct measurement of ΔH in ITC includes effects from dilution heat, binding heat, the energy required for desolvation and the energy change after protein rearrangement [99]. Therefore enthalpy obtained from ITC must be scrupulously analyzed and it is prudent to consider it an 'apparent enthalpy' while the contributions of its various components are separated and understood. ITC is therefore a very useful tool for complete thermodynamic characterization of small molecule interactions.

The stoichiometry and association constant (K_a) is determined by titration. From the association constant the change in Gibbs free energy (ΔG) is then calculated, and subsequently the change in entropy (ΔS). The heat capacity (ΔC_p) can be determined by performing the experiments at several different temperatures. This wealth of information provides a comprehensive characterization of bi-molecular interaction. ITC is considered the gold standard of kinetic measurement techniques as many new applications are validated by direct comparison with ITC reported findings.

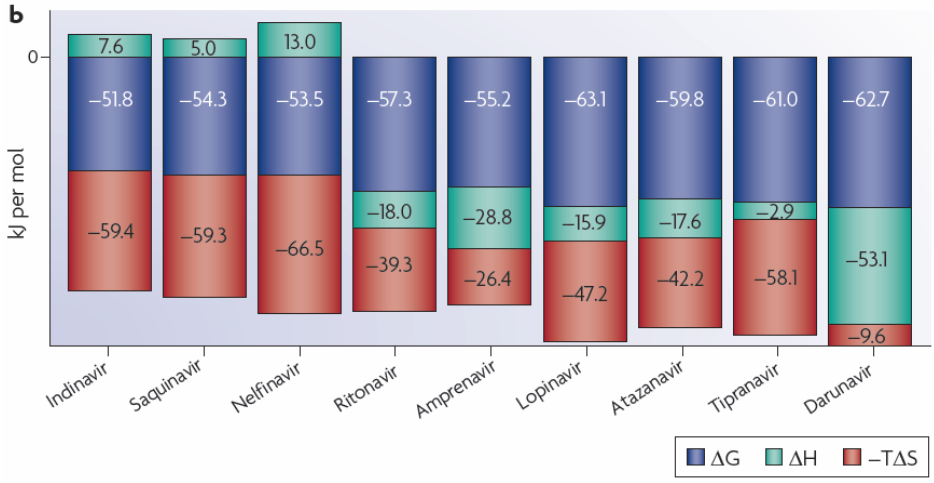

Figure 6. Thermodynamic profile of the binding of a series of small molecule inhibitors to HIV protease. The inhibitors were designed to optimize the enthalpic contribution to the binding energy. {REF Nature Protocols}

There are hundreds of reported small molecule-binding ITC experiments. The Journal of Molecular Recognition has published several reviews that summarize and highlight some of the important work in this field [100, 101]. Additionally, the Biotechnology Journal [97] and Methods in Enzymology [102] have recently published reviews as well.

While calorimetry is one of the foremost techniques for characterizing bi-molecular interactions, ITC typically requires 10-1000 μg of the binding partners. Concentration requirements and data quality are a primary consideration for ITC experiments, as concentrations of the reagents must be matched to both the affinity and the enthalpy change [103]. The concentration of reactants is increased to compensate for small changes in reaction enthalpy. However, there is a requisite range of concentrations that must be measured to ensure good accuracy in kinetic measurements. This problem is exemplified when measuring weak affinities and low available of reactants, such as T cell receptors binding to major histocompatibility

complex proteins. The precise determination of binding affinity is very difficult below the nanomolar level [104]. Displacement titration, a new mode of ITC has been developed in recent years to determine affinities down to the picomolar range [105]. Additionally, the ITC is a very low-throughput method. Current instruments boast a throughput of 75 binding experiments per day [106], which cannot be considered as 'high-throughput.' ITC is best used as a post-screening analysis step, in which the affinity of a small molecule to a target can be quantified and optimized based its thermodynamic profile (Figure 6).

2. SURFACE PLASMON RESONANCE

2.1 Introduction

The SPR phenomenon may be considered an energy matching condition between free electrons (e.g. a metallic sensor surface) and incident electromagnetic radiation (e.g. light coupled through a prism to the sensor surface). Researchers have used the SPR phenomena to investigate various physical properties of ultra-thing organic films [107], evaluate conducting polymers [108], detect pathogens in food and water [109], and discover novel pharmaceutical drugs [110]. The accumulation of surface-bound mass, particularly at high densities, will change the local refractive index condition and generate a measurable SPR signal. Accordingly, a major application of SPR sensors includes the measurement of binding affinities between small molecules and surface-bound receptors. Neither the small molecules nor the ligands require labels. Another advantage of SPR is the ability to monitor binding events in real-time; providing valuable kinetic information that many other techniques cannot measure.

2.2 Theory of Surface Plasmons

Informed by physical theories and mathematical models, a scientist approaches each experiment with an expectation of the outcome. However, formulas are often accurate to only a first approximation; the more general the model the more ideal the experimental system must be. Researchers rely on empirical coefficients, calibration constants, and physical equivalents to modify formulas for the nitty-gritty of practical application. Additionally, the list of assumptions and approximations used to make a model applicable can become alarmingly long. It is necessary to rigorously examine these assumptions to ensure proper employment of the theory.

Maxwell's equations form one of the most common models used to describe the behavior of electromagnetic radiation. Manipulating the angle of incidence of electromagnetic radiation on the boundary of two (semi-infinite) media bounded by a planar boundary of infinite extent (Figure 7) can generate phenomena described by familiar terms such as Snell's Law and the Brewster Angle. More unfamiliar EM behavior, such as surface plasmons, can also be understood through Maxwell's theory.

2.2.1 Dispersion Relation of Surface Plasmons

Consider an electromagnetic plane wave incident on the boundary described above. At any instant in time this wave can be described by the instantaneous electric $\boldsymbol{\mathcal{E}}$ and magnetic $\boldsymbol{\mathcal{H}}$ fields in each medium, respectively.

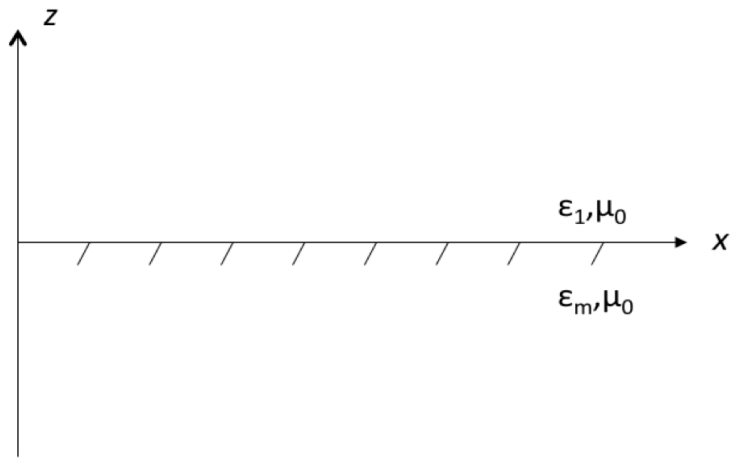

Figure 7. Definition of axis system and constitutive parameters

For $z < 0$

$$\boldsymbol{\mathcal{E}_1} = (\hat{a}_x E_{x1} + \hat{a}_z E_{z1}) e^{j(\omega t - k_{x1} x + k_{z1} z)} \tag{7a}$$

$$\boldsymbol{\mathcal{H}_1} = \hat{a}_y H_{y1} e^{j(\omega t - k_{x1} x + k_{z1} z)} \tag{7b}$$

For $z > 0$

$$\boldsymbol{\mathcal{E}_2} = (\hat{a}_x E_{x2} + \hat{a}_z E_{z2}) e^{j(\omega t - k_{x2} x - k_{z2} z)} \tag{8a}$$

$$\boldsymbol{\mathcal{H}_2} = \hat{a}_y H_{y2} e^{j(\omega t - k_{x2} x - k_{z2} z)} \tag{8b}$$

The amplitudes of the electric and magnetic fields are represented by *E* and *H*, respectively. The angular frequency is ω, *k* is the wave vector, and $j = \sqrt{-1}$. The fields described by equations (7ab) and (8ab) must satisfy Maxwell's equations:

$$\nabla \times \boldsymbol{\mathcal{E}} = -\boldsymbol{\mathcal{M}}_i - \mu \frac{\partial \boldsymbol{\mathcal{H}}}{\partial t} \tag{9}$$

$$\nabla \times \boldsymbol{\mathcal{H}} = -\boldsymbol{\mathcal{J}}_i + \sigma \boldsymbol{\mathcal{E}} + \varepsilon \frac{\partial \boldsymbol{\mathcal{E}}}{\partial t} \tag{10}$$

$$\nabla \cdot \mathfrak{D} = \varepsilon \nabla \cdot \boldsymbol{\mathcal{E}} = \boldsymbol{q}_{ev} \tag{11}$$

$$\nabla \cdot \mathfrak{B} = \mu \nabla \cdot \boldsymbol{\mathcal{H}} = \boldsymbol{q}_{mv} \tag{12}$$

For these expressions to be valid, it is assumed that the field vectors are single-valued, bounded, continuous (including their derivatives) functions of position and time. The boundary conditions are required to describe any variations of the field vectors at the interface of the two media. The boundary conditions for finite conductivity media in the absence of charges include:

$$\hat{n} \times (\boldsymbol{\mathcal{E}}_2 - \boldsymbol{\mathcal{E}}_1) = 0 \tag{13}$$

$$\hat{n} \times (\boldsymbol{\mathcal{H}}_2 - \boldsymbol{\mathcal{H}}_1) = 0 \tag{14}$$

Applying Maxwell's equations and the boundary conditions to the expressions for the electric and magnetic fields yield the dispersion relation for the planar interface between two semi-infinite media:

$$\frac{k_{z2}}{\varepsilon_2} + \frac{k_{z1}}{\varepsilon_1} = 0 \tag{15}$$

The wave vectors in the *x*- and *z*-directions are related by:

$$k_x^2 + k_{zi}^2 = \varepsilon_i \omega^2 \mu_0, \qquad i = 1,2 \tag{16}$$

From equations (11) and (12) the wave vector k_x is continuous across the interface. The wave vectors in the $\hat{x}$ and $\hat{z}$ directions can be rewritten as a function of the constitutive parameters and angular frequency of the incident electromagnetic radiation:

$$k_x = \frac{\omega}{c}\sqrt{\frac{\varepsilon_1 \varepsilon_2}{\varepsilon_1 + \varepsilon_2}} \tag{17}$$

$$k_{zi} = \frac{\omega}{c}\frac{\varepsilon_i}{\sqrt{\varepsilon_1 + \varepsilon_2}} \tag{18}$$

Now let us assume that medium 2 is air ($\varepsilon_2 = 1$), the angular frequency ω is real, and medium 1 is a metal such as Au or Ag with a complex permittivity ($\varepsilon_1 = \varepsilon_1' + \varepsilon_1''$). The expressions for the field vectors become imaginary or complex. The wave vector in the x-direction can be written as $k_x = k_x' + k_x''$ where

$$k_x' = \frac{\omega}{c}\sqrt{\frac{\varepsilon_1' \varepsilon_2}{\varepsilon_1' + \varepsilon_2}} \tag{19}$$

$$k_x'' = \frac{\omega}{c}\frac{(\varepsilon_1 + \varepsilon_2)^{1/2}}{2(\varepsilon_1 \varepsilon_2)^{1/2}}\frac{\varepsilon_1'' \varepsilon_2^2}{(\varepsilon_1' + \varepsilon_2)^2 + \varepsilon_1''^2} \tag{20}$$

The free valence electrons of a metallic solid can be viewed as an electron "gas" that permeates the crystal lattice of the metal. The dielectric function of the electron gas depends strongly on the applied frequency of modulation. The long wavelength dielectric response of an electron gas is obtained from the equation of motion of a free electron in an electric field. For frequencies of modulation less than the plasma frequency of the metal, the permittivity of the metal can be written as:

$$\varepsilon(\omega) = 1 - \frac{\omega_p^2}{\omega^2} \tag{21}$$

The plasma frequency is defined as $\omega_p^2 \equiv ne^2/\varepsilon_0 m$ where n is the bulk electron density, and e and m are the charge and resting mass of an electron, respectively. The dispersion relation for the surface plasmon can be rewritten as:

$$\omega_{sp}^2 = \frac{\omega_p^2}{2} + c^2 k_x'^2 - \sqrt{\frac{\omega_p^4}{4} + c^4 k_x'^4} \tag{22}$$

The dispersion relation of a surface plasmon is plotted in Figure 8. It is important to recognize that electromagnetic radiation travelling in an arbitrary direction in medium 2 ($k_x = \sqrt{\varepsilon_2} w/c$) cannot simultaneously provide the correct wave vector and angular frequency to excite a surface plasmon. Furthermore, surface plasmons cannot spontaneously transform into light.

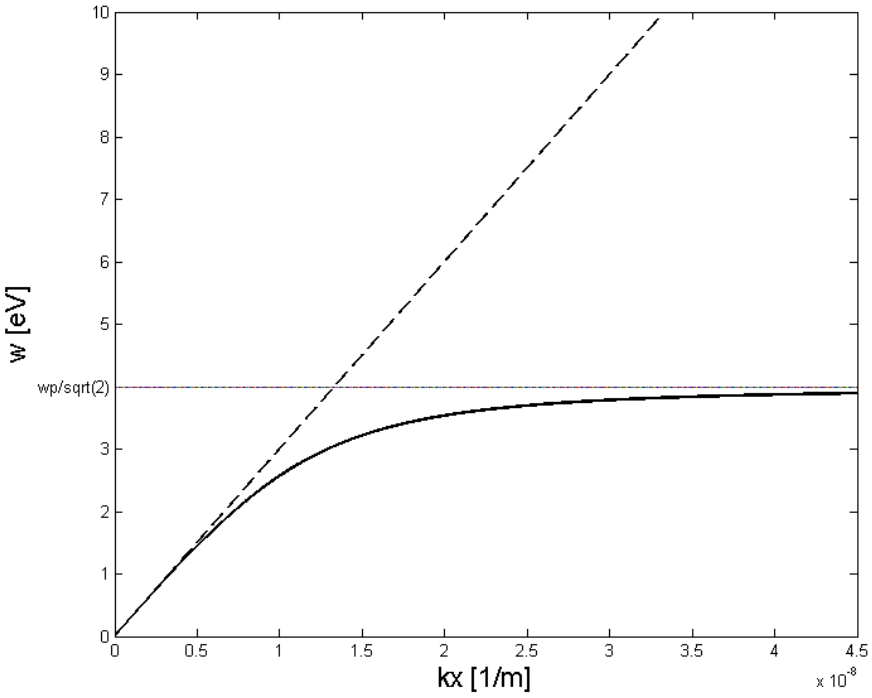

Figure 8. The dispersion relation for non-radiative surface plasmons at the interface of Au and air (solid line). The surface plasmon never intersects the light line (dashed line) and therefore cannot transform into light. At short wavelengths, the surface-plasmon dispersion curve approaches asymptotically the non-retarded surface plasmon frequency ($\omega_{sp} = \omega_p/\sqrt{2}$).

2.3 Properties of Surface Plasmons

2.3.1 Propagation Length

Metals and certain doped semiconductors ($\varepsilon_1' < 0$ and $|\varepsilon_1'| > \varepsilon_2$) allow for a real $k_x'$to propagate at the interface of the two media. The length of propagation is determined by

imaginary part of the wave vector in the *x*-direction given by equation (20); the length *L* after which the intensity of the SP decreases to 1/*e* is given by:

$$L = \frac{1}{2k_x''} \tag{23}$$

2.3.2 Spatial Extension

The imaginary wave vectors given by (12) describe a wave tightly bound the interface between mediums one and two. The skin depths into mediums 1 and 2 are given by:

$$z = \frac{1}{|k_{zi}|} \; or \; z = \begin{cases} \frac{\lambda}{2\pi}\sqrt{\frac{\varepsilon_1' + \varepsilon_2}{\varepsilon_2^2}}, & z > 0 \\ \frac{\lambda}{2\pi}\sqrt{\frac{\varepsilon_1' + \varepsilon_2}{\varepsilon_1'^2}}, & z < 0 \end{cases} \tag{24}$$

A wave that propagates at the interface and decays exponentially in directions normal to that interface is known as an 'evanescent wave.' There is no real power transferred from medium 1 across the boundary.

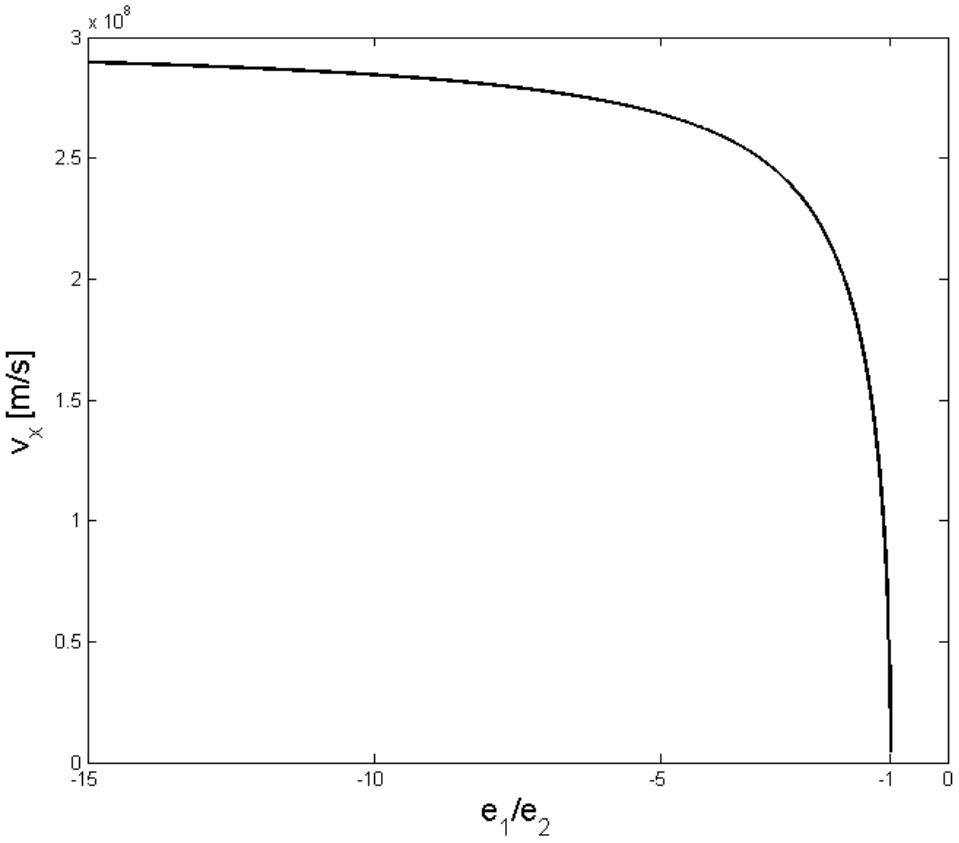

Figure 9. As ε_1 approaches $-\varepsilon_2$, the group and phase velocities go to zero, the wave vector k_x goes to infinity, and the wavelength of the surface plasmon approaches zero. The surface plasmon resembles localized fluctuations of the electron plasma.

2.4 Excitation of Surface Plasmons

Surface plasmons on a thin metallic film can be directly excited by the transfer of momentum from incident electrons to the electrons of the solid. Incident electrons are scattered by the film, and depending on the angle of the scattered electron, the momentum of the incident

electron matches the dispersion relation of the surface plasmon. Electrons have been used to study the physics of SP at large ($k_x > \omega_p/c$) values.

Photons can be used to excited surface plasmons as well. It is not possible to directly excite surface plasmons on a thin surface with photons. At a given photon energy ($\hbar\omega$), the incident wavevector ($\hbar\omega/c$) must be increased by Δk_x. Two popular methods used to supply the requisite Δk_x are the grating coupling and Attenuated Total Reflection (ATR).

2.4.1 Grating Coupler

Light incident on a plasma surface with a grating constant *a,* at an angle θ will have a wavevector component parallel to the surface of the form:

$$k_x = \frac{\omega}{c}\sin\theta \pm n\frac{2\pi}{a}, \qquad n = 0,1,2 \ldots \tag{25}$$

The dispersion relation given by equation (15), is thus satisfied

$$k_x = \frac{\omega}{c}\sin\theta \pm \Delta k_x = \frac{\omega}{c}\sqrt{\frac{\varepsilon_1'\varepsilon_2}{\varepsilon_1' + \varepsilon_2}} \tag{26}$$

The resonance condition can be observed as a minimum of reflected light. The height of the amplitude grating determines the magnitude of this minimum. Surface plasmons excited in this manner may release their energy in the form of the re-radiation of light via the coupling method of the grating.

2.4.2 ATR Coupler

The Attenuated Total Reflection coupling method is currently the most common technique for the excitation of surface plasmons in SPR-based applications. ATR methods use a

prism to couple the evanescent wave to the surface plasmon energy condition on a metallic surface. An example ATR configuration is shown in Figure 10.

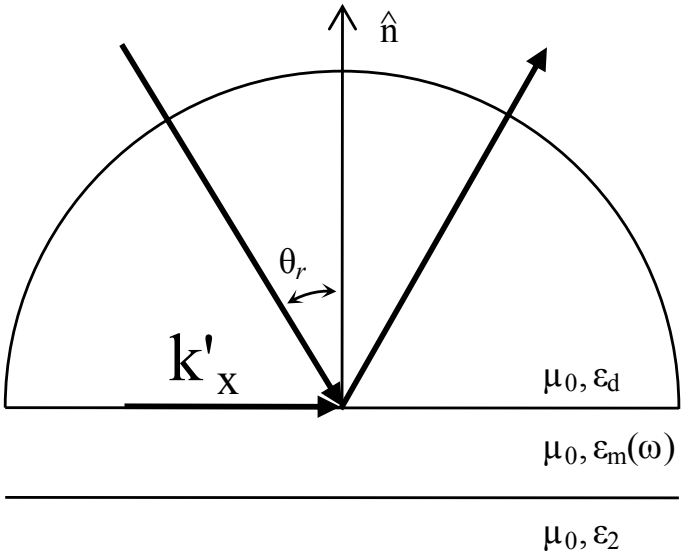

Figure 10. The excitation of surface plasmons via the Kretschmann coupling method.

As incident light ($k = \omega/c$) passes through a medium with $\varepsilon_d > 1$(*e.g.* quartz prism) its momentum increases to $\sqrt{\varepsilon_d}\hbar\omega/c$ and its projection on the surface of the film becomes:

$$k_x = \frac{\omega}{c}\sqrt{\varepsilon_d}\sin\theta \tag{27}$$

With this increase in Δk_x, the light line in Figure 11 can match the dispersion relation of the surface plasmon on the interface between the metal and air.

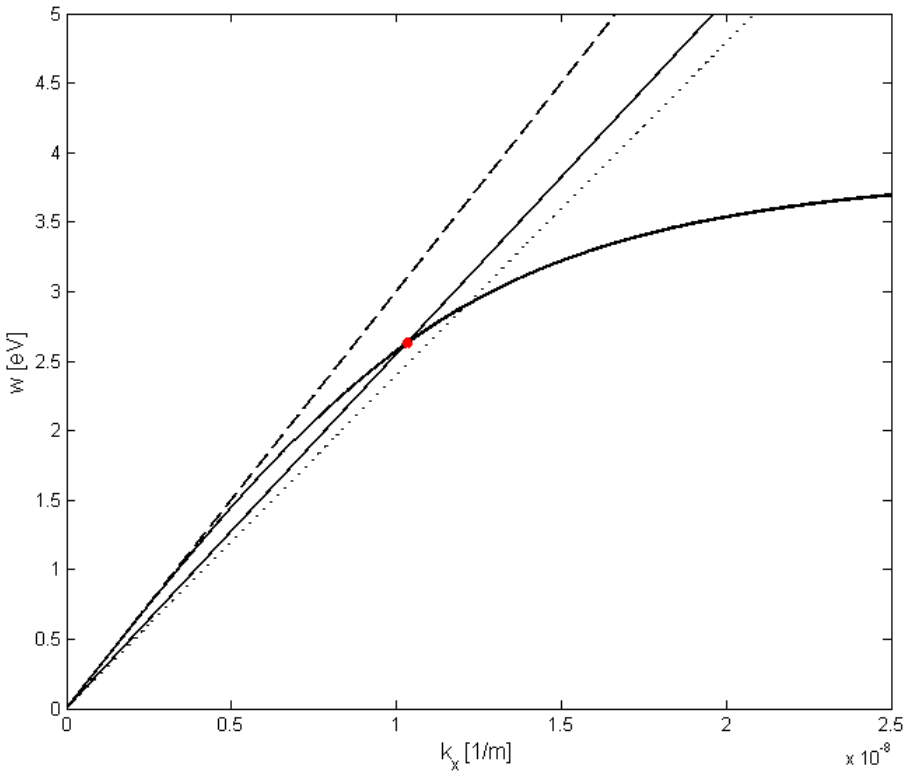

Figure 11. Dispersion relation of surface plasmons in the ATR coupling method. The intersection of the two solid lines represents the excitation of a surface plasmon using the angle of incidence to satisfy the wavevector mismatch.

It is possible to match the dispersion relation of equation 15 by manipulating the angle of incidence to achieve surface plasmon resonance:

$$\theta_r = \sin^{-1}\sqrt{\frac{\varepsilon_1'\varepsilon_2}{(\varepsilon_1' + \varepsilon_2)\varepsilon_d}} \tag{28}$$

This is angle is known as the resonance angle and corresponds to a minimum in the intensity of reflected light.

Two popular ATR coupling methods were developed by Otto and Kretschmann, respectively. The Otto configuration [111] introduces a dielectric layer between the prism and the metallic surface, while the Kretschmann configuration [112] places the metallic film directly on the prism surface. The gap thickness in the Otto configuration determines the strength of the energy coupling. A typical dielectric thickness of 0.5 m is used on an Au film illuminated with 632.8nm light [113]. The Kretschmann configuration is most often preferred over the Otto configuration and is pictured in Figure 10. (Unless explicitly stated, any model SPR platform discussed in the follow text may be assumed to be in the Kretschmann configuration.)

Other methods for exciting surface plasmons include optical fibers and alternating layers of dielectric around a metallic core. EM radiation traveling through a gold-coated optical fiber can excite surface plasmons on the fiber's surface, allowing for a probe to be used at a distance from the light source and detector [114]. Long range surface plasmon resonance (LRSPR) detectors have a metallic layer sandwiched between two identical dielectric layers [115]. The reflected illumination intensity changes dramatically as a function of illumination angle in LRSPR detectors, but this increased sensitivity comes at the cost of reduced spatial resolution.

3. SPR BIOSENSORS

3.1 Introduction

Surface plasmon resonance (SPR) is a prevalent label-free biosensor technology routinely exercised in bio-affinity studies [116], clinical diagnostics [110], and environmental analysis [117]. Perhaps one of its biggest advantages over related techniques is its sophisticated characterization of bimolecular reaction kinetics.

3.2 Materials & Methods

The most popular SPR biosensor is based on the Kretschmann configuration (Figure 10). The sensor surface is comprised of a thin metal film (~45nm of gold) on the top face of a prism. In flow-base assays, the gold film represents one of the boundaries of a microfluidic channel, which is used to deliver sample to the surface (and quickly remove it after dissociation). An LED or laser diode illuminates the film through the prism. At a particular angle of incidence, the electromagnetic radiation from the light source couples with the free electrons on the film surface, resulting in a decrease in reflected light, usually measured by a CCD camera or photodiode. Changes in the refractive index on the sensor surface (*e.g.* binding of an analyte from solution) change the coupling condition and the resonance angle. Most commercial SPR systems illuminate the sensor surface a fixed angle and measure changes in signal intensity.

3.2.1 Sensitivity

The optimization of an SPR optical biosensor is informed by the desired measurement functionalities; tradeoffs between various characteristics of the instrumentation, such as spatial resolution v. surface sensitivity, may limit the possible measurements available to a particular SPR platform configuration. Chinowsky et al. identify four major attributes of an SPR biosensor

available for optimization [118]: (1) refractive index resolution, (2) spatial resolution, (3) refractive index range, and (4) mechanical and optical simplicity. The proposed experiment will dictate the relative importance of these parameters. In general, maximizing the signal to noise ratio (SNR) is the first step in designing an SPR system.

3.2.2 Signal to Noise Ratio in SPR Imaging

The signal in an SPR imaging system is the change in measured light intensity (as a function of changing refractive index located within the surface-bound evanescent wave). The signal S from an SPR imager may be written as:

$$S = \frac{d(I \times R)}{dn} \Delta n = I \times \frac{dR}{dn} \times \Delta n \tag{29}$$

where I is the illumination intensity (units of photoelectrons), Δn is the change in refractive index, and dR/dn is the derivative of reflectivity with respect to surface refractive index. Sources of noise include reset noise, output amplifier noise, dark current noise, and photo response non-uniformity [119]. Statistical fluctuations in the number of photons incident on the imaging detector is known as shot noise. This fundamental limit on noise performance in light detection systems tends to dominate in bright imaging systems and can be written as:

$$\sigma = \sqrt{I \times R} \tag{30}$$

We can express the signal to noise ratio (SNR) as:

$$SNR = \frac{S}{\sigma} = \sqrt{I} \times \frac{dR}{dn} \times \frac{\Delta n}{\sqrt{R}} \tag{31}$$

For small changes in R, this equation reduces to:

$$SNR = \sqrt{I} \times \frac{dR}{dn} \tag{32}$$

Given our assumptions, the SNR is improved by increasing the illumination intensity and increasing the change in reflectivity with respect to changing refractive index.

3.2.3 Camera Noise Analysis

Increasing illumination intensity may require changes to the light detector. For example, the saturating limit of the number of photoelectrons could be increased. Increasing the pixel size or the image acquisition rate will increase this limit.

There are several characteristics to consider when evaluating an image detecting system for use in SPR imaging. The relative importance of the number and size of pixels, frame rate, uniformity and dark current, and cost must be considered when designing an SPR platform. CCD cameras balance these components and are a popular image detector choice. The performance of a CCD camera may be limited by temporal or spatial noise sources. The relative levels of signal noise for two cameras are plotted in Figure 12.

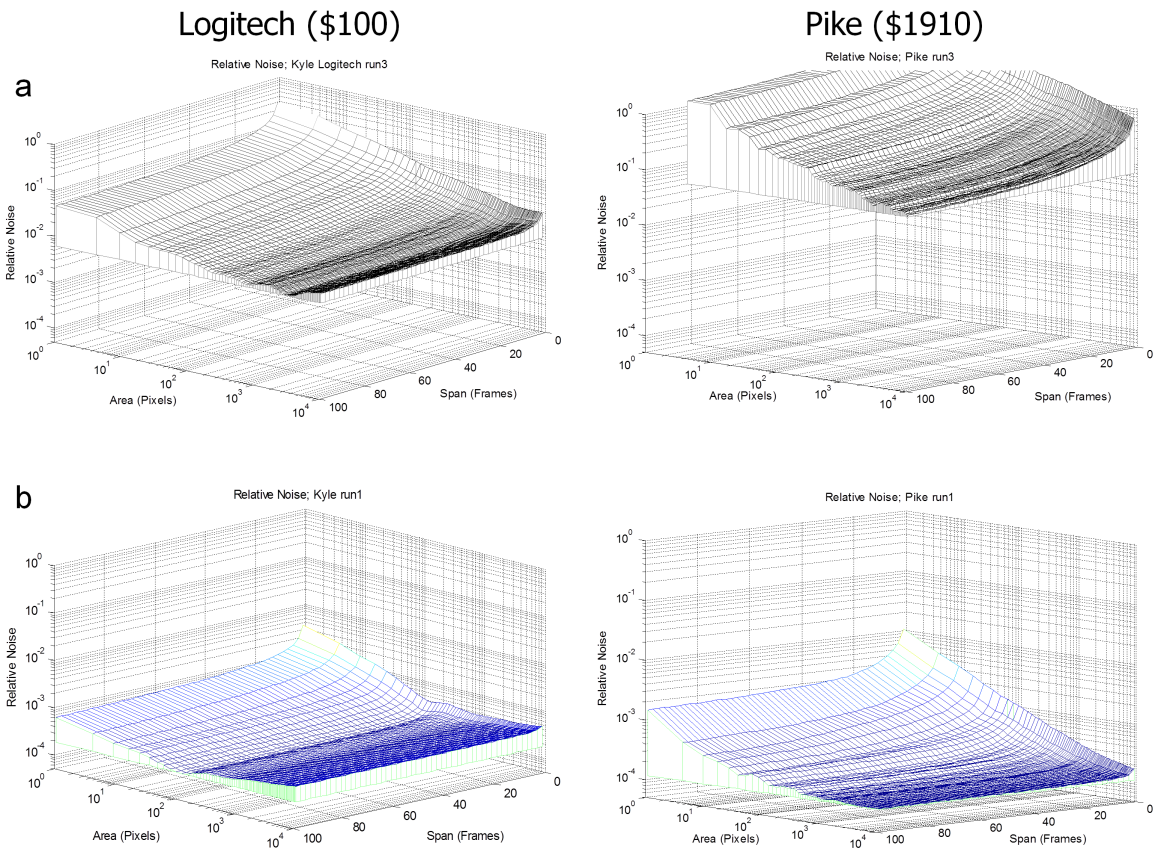

Figure 12. Noise analysis for two cameras at (a) high illumination intensities, and (b) low illumination intensities. Relative noise is defined as the mean pixel value divided by the standard deviation of all pixels values. Generally, the noise is inversely proportional to the number of pixels in the detection area and number of images collected. Each camera was exposed to the same light source and captured images at 30 frames per second.

3.2.4 Reflected Light Intensity

Optimizing the reflected light component of the SPR signal may be achieved through careful manipulation of the materials and geometry of the SPR platform. Three interrelated

variables to balance are light source wavelength, Au sensor thickness, and illumination angle. Unless otherwise stated, the parameters for the following Winspall simulations [120] are: 42 nm Au film thickness, BK7 'half cylinder' prism, 632.8 nm p-polarized light.

The wavelength of the light source is selected first when building an SPR detector. The slope of the reflectance as a function of angle of incidence in a Kretschmann configuration is maximized at longer wavelengths of light (Figure 13). For small changes in refractive index, $dn = d\theta$.

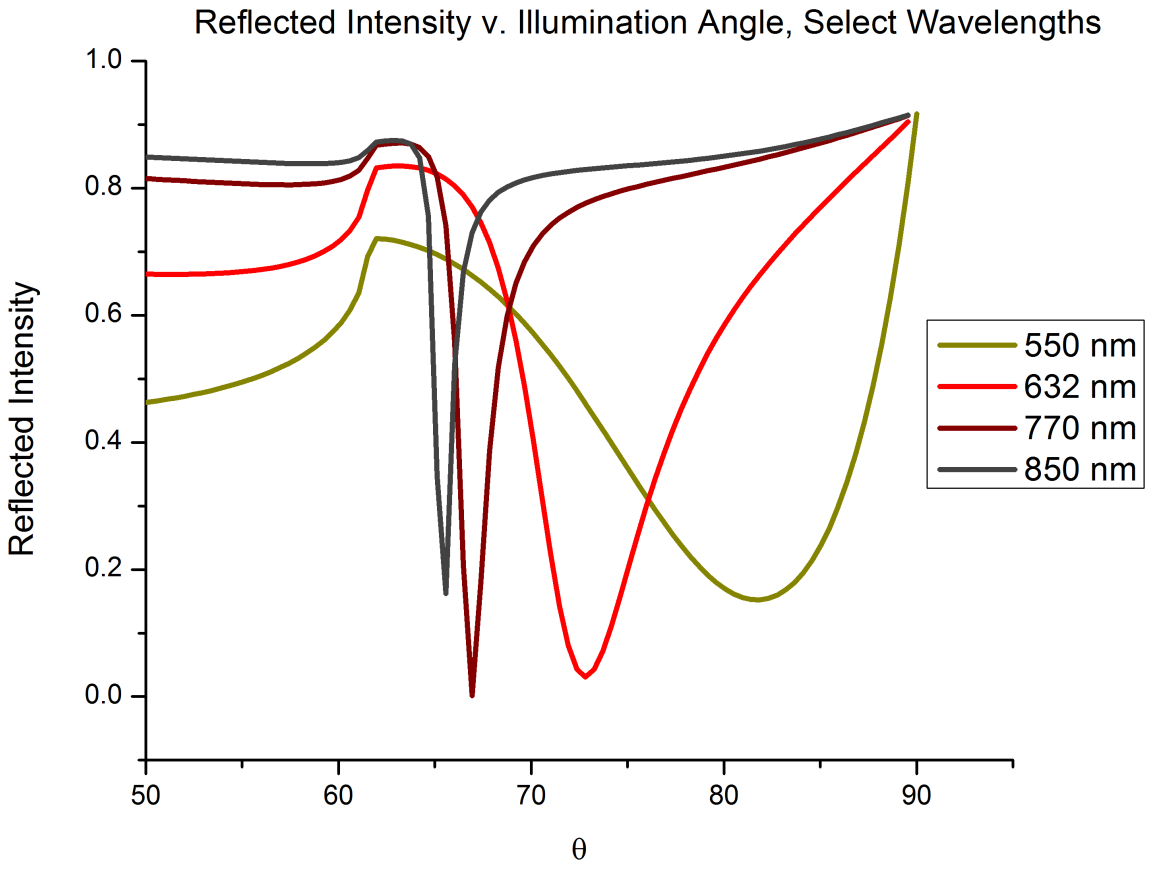

Figure 13. Reflected light intensity as a function of illumination angle for several frequencies of incident light. The SPR "dip" profile narrows as the wavelength of light increases, corresponding to a larger change in intensity for small changes in resonance angle (or dn). The surface plasmon propagation length and penetration depth into the bulk also increase according to wavelength; this decreases spatial resolution and reduces the relative contribution of the sensor surface to the total SPR signal.

The appropriate thickness of the Au sensor chip is determined by the wavelength of the light source. The Au chip is fabricated in a clean room environment and is consumed at the conclusion of each experiment. A typical thickness of an Au film is 40-50 nm.

For fixed-angle SPR experiments, the selection of an appropriate angle is required; the angle of incidence (illumination angle) may be varied to optimize the change in signal. This final signal is a function of sensitivity (light intensity from $dR/d\theta$) and its amplification from camera gain. This relationship is plotted in Figure 14.

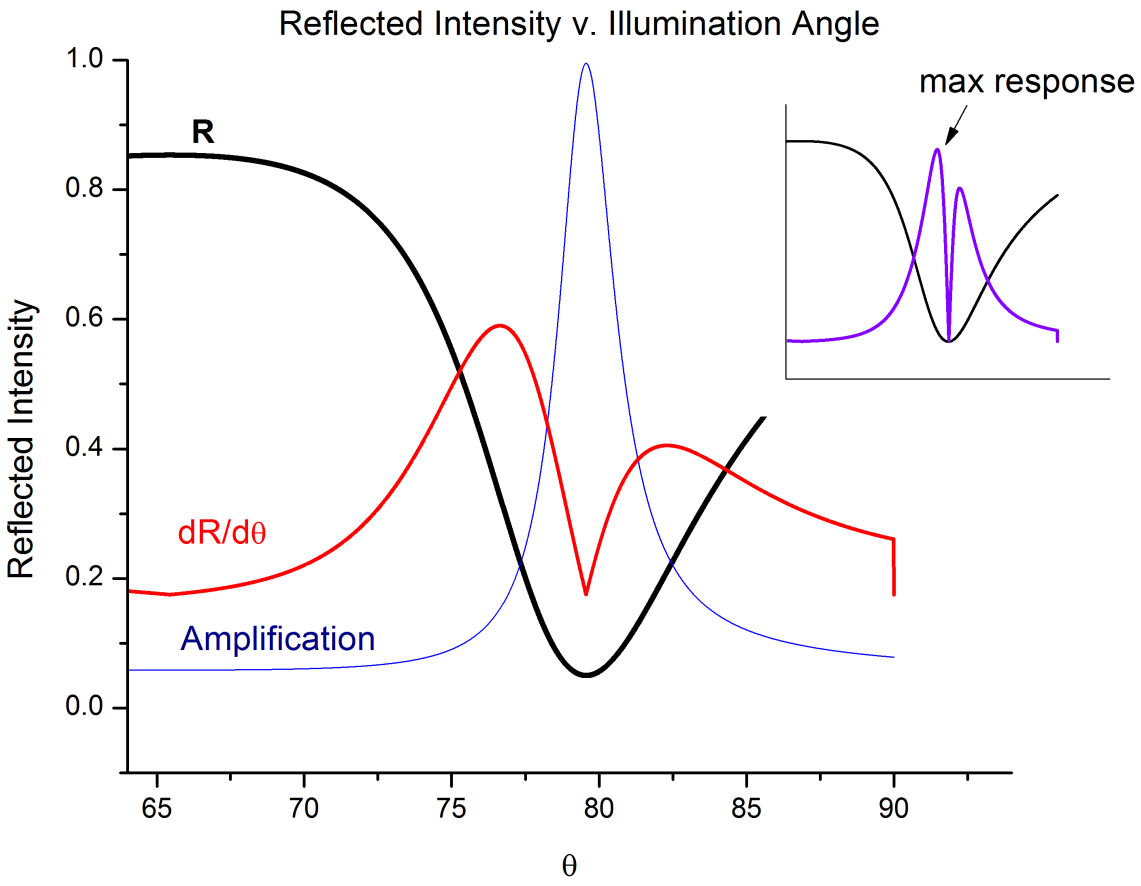

Figure 14. The selection of the angle of illumination for fixed-angle measurements is informed by the magnitude of response at each angle. The reflectance is plotted in black and the absolute magnitude of its derivative is plotted in red. The sensitivity of the SPR response may also be influenced by the amount of gain or amplification available at a particular angle of incidence (blue line). The amplification is assumed to be 80% of the camera saturation value and is plotted as 0.8/R. [inset] The maximum response angle corresponds to the maximum of the product of the slope and amplification (purple line).

Generally, the collected light intensity is amplified to no more than 80% of a CCD camera's saturation level to preserve signal quality. The sensitivity drives the bulk of the SPR response and is shown for a fixed angle measurement of Bovine Serum Albumin collecting on a sensor surface in Figure 15.

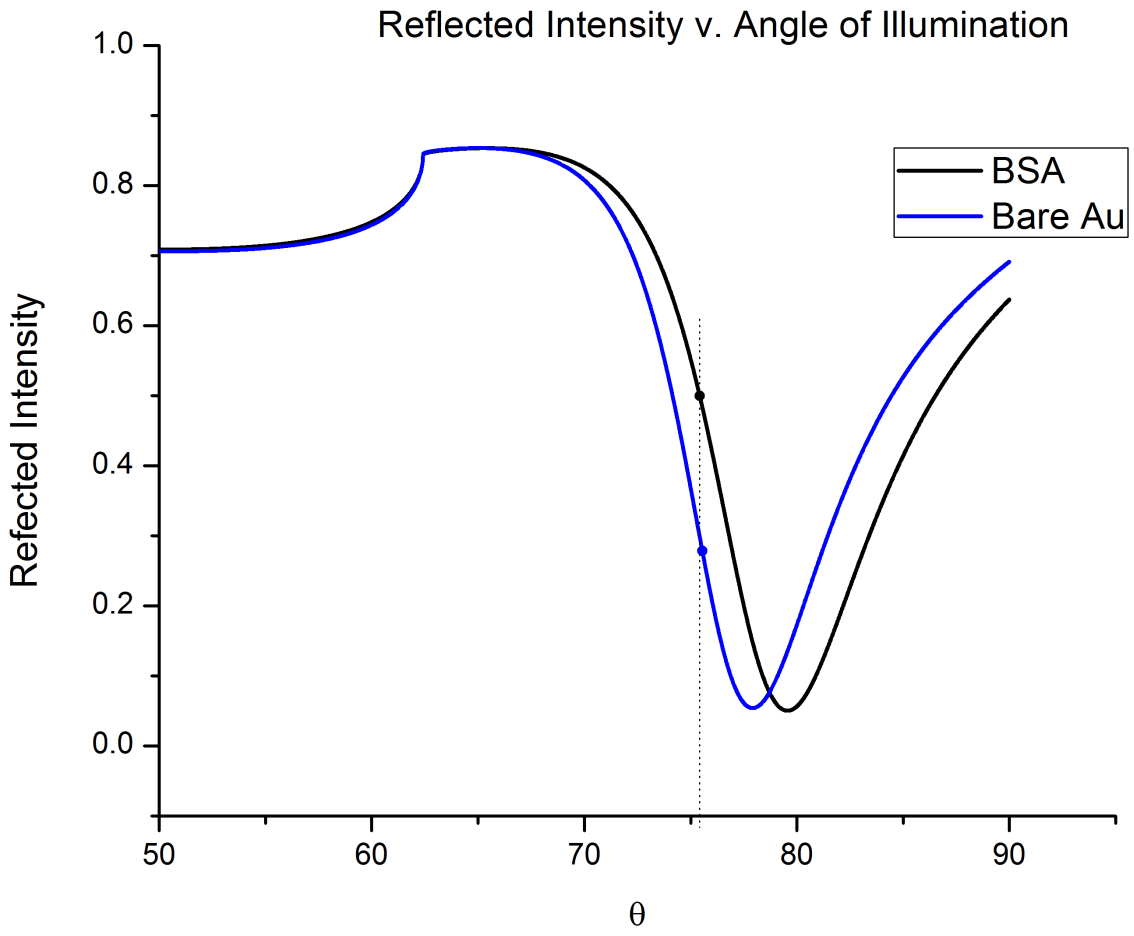

Figure 15. SPR response due to surface-bound Bovine Serum Albumin. At a fixed angle of observation, the reflected light intensity changes due to the presence of a monolayer of immobilized protein with a different refractive index than the bare Au.

3.2.5 Mass Sensitivity

The sensitivity of the SPR signal to the local environment of the sensor surface is primarily used to measure interactions between two binding partners. Stenberg et al. have quantified the correlation between surface concentration of protein on the biospecific active surface and SPR response with radiolabeled proteins [121]. In a typical Biacore SPR instrument (which represented 87% of the reported SPR instruments in 2005) [122], a 122 mDeg shift in resonance angle corresponds to a mass density change of 1 ng/mm^2. Biacore instruments often measure the SPR signal in response units (RU). 1 mDeg is equal to 8.2 RU (and varies slightly according to SPR configuration details). Current commercially available SPR platforms can achieve 0.1 mDeg sensitivity, which corresponds to a mass sensitivity of ~1pg/mm^2. The mass sensitivity can be dramatically improved by imaging the SPR sensor surface; the laboratory of NJ Tao has SPR microscopy platforms with reported mass sensitivities of 0.2 fg/mm^2. The high spatial resolution reduces the inherent spatial averaging in reported Biacore mass sensitivities. Some research groups quantify the mass sensitivity of their instruments by reporting the mass of the smallest they can detect; David Myszka has published several papers characterizing the interaction between Carbonic Anhydrase II with many small molecules (95-500 Da) [123].

Changing the refractive indices of the prism and materials used, using silver instead of gold, and using different frequencies of light all change the sensitivity of the SPR detection platform.

3.2.6 Surface Chemistry

The surface chemistry of the sensor surface is a pivotal variable for SPR assays. A variety of molecular structures in the form of linkers, blockers, and conductors have been

developed to work with gold, which is the most commonly employed sensor surface. The conventional SPR signal does not discriminate between different molecules adsorbing on its surface; it is only sensitive to changes in mass density. Therefore, the sensor surface must be well characterized before it can be used to generate high quality data.

Preventing nonspecific adsorption of analytes to the sensor surface is a primary goal of manipulating the sensor surface chemistry. If a molecule binds to the sensor, it should only bind to its partner, ensuring the measured kinetics are representative of the bimolecular binding. This can be achieved by immobilizing a monolayer of polyethylene glycol, which blocks adsorption to the gold by presenting a hydrophilic screen to wayward analytes in solution. A small fraction of the PEG molecules can be terminated with COOH or NH_2 groups that may be used in amine coupling. Dextran, a polysaccharide of many glucose molecules, is another popular surface chemistry. It too forms a monolayer on the surface, but extends much further from the surface (typically ~100nm) and has multiple locations on each strand to immobilize a ligand. When two molecules interact in solution, the orientation of binding sites and frequency of collision will affect the reaction rate. Immobilization of a binding partner to a dextran polymer will imperfectly simulate the reaction conditions found in solution-based measurements [124]. The observed rate constants in this system will generally be lower than those measured in solution-based interrogations. To this end, it is important to maintain constant viscosity in the matrix.

3.2.7 SPR Kinetic Theory

Surface plasmon resonance (SPR) is routinely used in bio-affinity studies [125], clinical diagnostics [126], and environmental analysis [12]. SPR can be used to monitor molecular binding events, as its real-time output facilitates kinetic binding measurement (i.e. association

and dissociation rate constants) in high-throughput environments (e.g. imaging [127], microarrays [128]). The need for detailed kinetic binding and thermodynamic information in modern drug discovery has established SPR as a prominent label-free technology for fragment-based drug discovery and small molecule binding analysis [129].

The kinetic binding information measured by SPR is crucial component for relating the structure of biological molecules to their function. Designing high quality experiments is difficult and the data must be evaluated with a skeptical eye. Myszka describes the limitations of post-experiment kinetic analysis; explaining a good fit to the binding data does not ensure that the binding reaction model is correct [130]. Appropriate experimental variables such as flow rate, surface density, and contact time may be manipulated to validate the choice of a particular reaction model. Additionally, interactions should be studied with each reactant independently immobilized on the sensor surface to block the experiment artifacts associated with immobilization, the equilibrium constant calculated from the measured rate constants should be compared to an experimental measurement of K_D, and the same reaction should be measured with solution-based [131] interaction technologies [132] for a comprehensive evaluation of kinetic data.

SPR based biosensors can be used to measure the kinetics of the reversible binding of an analyte of species *A* from solution to a binding site of species *B* immobilized on the sensor surface. The binding stoichiometry that we will consider is defined as a 1:1 interaction model. It is analogous to the Langmuir adsorption model, with three basic assumptions: (1) the adsorption cannot proceed beyond monolayer coverage, (2) all sites are equivalent and the

surface is uniform, and (3) the ability of a molecule to adsorb to a given site is independent of the degree of occupation of neighboring sites [133].

These assumptions are reasonable and can be verified for many different binding events. Information about the molecular architecture is used to verify the existence of a single binding site, for example. Studies using various microscopy techniques, such as Atomic Force [134] or Electron Diffraction [135], have independently verified the uniformity of binding sites and monolayer coverage for a multitude of surface chemistries. Additionally, intermediate layers of PEG or Dextran have been developed to prevent non-specific adsorption onto the sensor surface. Experimental protocols to tailor specific surface chemistries are widely available. Proper spacing between ligands or binding sites will obviate concerns about steric hindrances.

Our final assumption is that the analyte has a sufficiently high mass transport from the bulk to the sensor surface such that it does not limit the rate of binding. Reducing or eliminating the effects of mass transport is primarily achieved by increasing the flow rate in flow-based experiments and reducing the number of binding sites on the sensor surface. This assumption is validated after the experiment by plotting the SPR signal as a function of time, and will be addressed later.

For a bimolecular interaction between analyte A and ligand B yielding the complex C, the dynamic equilibrium is given by:

$$A + B \overset{k_a}{\rightarrow} C \tag{33}$$

$$C \underset{k_d}{\rightarrow} A + B \tag{34}$$

where the forward and reverse reaction rates are represented by the association rate constant k_a and the dissociation rate constant k_d, respectively. Based on our assumptions above,

k_a and k_d represent the second- and first-order reaction rates. The association process is described by:

$$\frac{d[C(t)]}{dt} = k_a[A(t)][B(t)] - k_d[C(t)] \tag{35}$$

As the analyte binds with the immobilized ligand, the number of binding sites disappears according to:

$$[B(t)] = -[C(t)] + [B_0] \tag{36a}$$

The number of analytes decreases in a similar manner.

$$[A(t)] = -[C(t)] + [A_0] \tag{36b}$$

The concentration of complexes a function of time can be rewritten as

$$\frac{d[C]}{dt} = k_a[C(t)]^2 + k_a([A_0] + [B_0]) \tag{37}$$

$$- [C(t)](k_a([A_0] + [B_0]) + k_d)$$

In flow-based SPR assay, the analyte is continuously replenished during the injection phase. Therefore, there is significantly more analyte in solution than ligand binding partners on the sensor surface ($A_0 \gg B_0 \therefore A_0 \gg C$). This is a fair assumption; the continuous flow of injection provides a steady amount of analyte in solution as the analyte on the surface is depleted. The rate of formation of the complex becomes:

$$\frac{d[C(t)]}{dt} = k_a[A]_0[B]_0 - [C(t)](k_a[A]_0 + k_d) \tag{38}$$

At t=0 the number of complexes C must equal zero. The growth and decay in the number of complexes follows an exponential curve. Any deviation from this characteristic shape suggests that the binding is not a 1:1 stoichiometry or that the reaction suffers from mass transport limitations.

Association

$$[C(t)] = \frac{k_a[A]_0[B]_0}{(k_a[A]_0 + k_d)}(1 - e^{-t(k_a[A]_0 + k_d)}) \tag{39}$$

Dissociation

$$[C(t)] = \frac{k_a[A]_0[B]_0}{(k_a[A]_0 + k_d)}e^{-tk_d} \tag{40}$$

The shift in the SPR resonance angle is proportional to the amount of bound mass, with a typical mass sensitivity factor [136] of 120 mDeg per 100 ng/cm^2. As was shown in Figure 15, the changing resonance condition due to accumulation of surface-bound mass will generate a change in reflected light intensity. Therefore, by monitoring the percentage change of intensity at a fixed angle, the SPR response can be used to extrapolate the kinetic parameters of the molecular binding. Global analysis [137], the process of simultaneously fitting association and dissociation kinetic data from an SPR biosensor, has been shown to accurately measure the kinetic binding constants of a binding event partially controlled by mass transport [138].

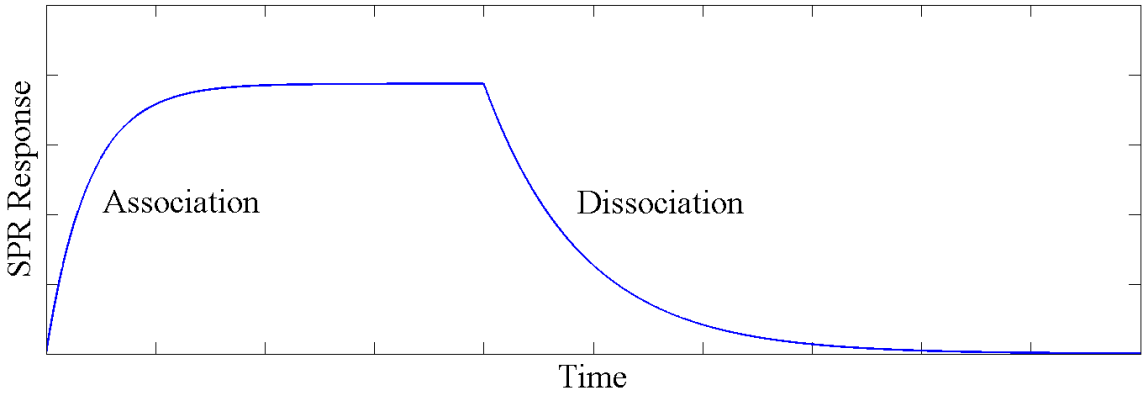

Figure 16. The change in light intensity at a fixed angle due to the association and dissociation of an analyte in solution and its binding partner immobilized on a sensor surface. The exponential growth and decay of this SPR sensorgram may be fitted with the association and dissociation equations above.

The association and dissociation rate constants can be calculated from the slope and intercept, respectively, of the dR_A/dt versus R_A plot, where R_A is the SPR response obtained from the kinetic curves after subtraction of the background signal [139]. Additionally, we can obtain K_D from a graph of the maximum SPR signal versus analyte concentration as shown in Figure 17.

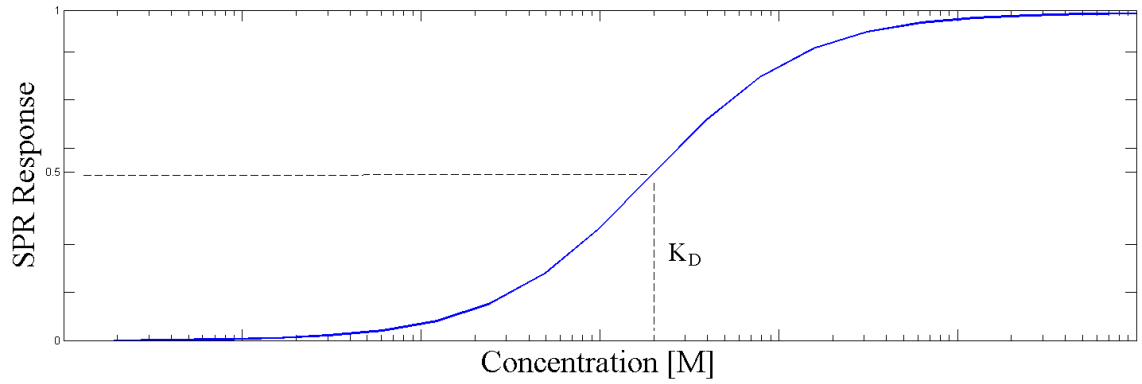

Figure 17. The dissociation constant K_D is the concentration of analyte that generates 50% of the saturated SPR signal.

There are two significant obstacles facing the current SPR detection paradigm for small molecule binding analysis: (1) mass sensitivity [140]: the mass ratio of the two binding partners is (empirically) limited to ≤ 2000, effectively limiting the mass of the smaller binding molecule to approximately ≥ 95 Da [123], and (2) mass transport limitation (MTL): the chemical process of association and dissociation can be influenced by dilatory mass transport of sample analytes to the sensing region, confounding the accuracy of kinetic rate constant measurement. (The latter obstacle may be considered a consequence of the mass sensitivity of SPR: the conventional strategy of decreasing the surface density of immobilized receptors to mitigate the effects of MTL simultaneously decreases the mass-dependent SPR signal.)

A number of recent publications have addressed the mass sensitivity constraints of SPR [141]; techniques such as plasmonic-based impedance sensors and SPR microscopy [142] employ novel detection strategies or improved optical systems to augment conventional SPR sensitivity. The theory of kinetic binding analysis has been rigorously examined: data from a

binding reaction that is partially limited by mass transport may be evaluated using various analysis methods such as global fitting but only if the kinetic model assumptions are satisfied [143-147]. There is little evidence of hardware improvement to increase the dynamic range of kinetic rate constants (k_a, k_d) measurement. The fluidic delivery system is not an ancillary component of a comprehensive SPR detection platform and warrants individual consideration.

4. FOUR-PORT MICROFLUIDIC FLOW-CELL WITH INSTANT SAMPLE SWITCHING

4.1 Introduction

In its most popular application, surface plasmon resonance (SPR) technology provides real-time measurement of the extent of solute adsorption to a sensor surface; the rates of association k_a [$Mol^{-1}s^{-1}$] and dissociation k_d [s^{-1}] between molecular binding partners can be extracted from an SPR signal. In general, the observed kinetic measurement data are a function of analyte mass transport and analyte/receptor binding affinity. The binding reaction is mass transport limited (MTL) if hydrodynamic forces retard the reaction rates of association and/or dissociation.

A common example of MTL occurs when the diffusion of the analyte near the sensor surface is comparable or slower than the binding of the analyte to the surface [130,148]. The delivery speed of analyte to the sensing region, before it diffuses to the sensor surface, is another potentially limiting factor. Although it is typically assumed to have a negligible effect in most popular kinetic binding models, this speed become important when the binding reactions have fast kinetics [143-147]. Small molecule binding reactions are less likely to be limited by slow diffusion rates than their large molecule analogues, as an analyte's diffusion coefficient scales inversely with its molecular weight ($D \sim 1/\sqrt[3]{MW}$). However, this increased diffusion rate during sample convection to the sensing region may limit the availability of a quickly associating analyte or prolong removal during the dissociation phase. The large dispersion rate and fast binding kinetics characteristic of small molecules make their measurement particularly susceptible to this type of MTL.

The no-slip boundary condition in viscous fluid flow restricts the velocity of a fluid immediately adjacent to a solid boundary, which can manifest as a parabolic fluid velocity profile in microfluidic tubing. As analytes randomly diffuse during transport they experience disparate convective forces according to their position in the tubing. Consequently, it takes a finite amount of time for the fluid in the sensing region to transition between 100% buffer and 100% sample. This 'transition' time (or injection rise and fall time) can limit the chemical reaction on the sensor surface by reducing the availability of analyte during the association phase (reducing measured k_a), or insufficiently removing unbound analytes during dissociation (reducing measured k_d). Formally, this type of MTL invalidates the 'continuously replenished analyte bulk concentration' assumption of popular kinetic analysis models [149]. A minimal transition time between buffer and sample solution on the sensor surface is necessary to measure the fast kinetic rates of bi-molecular interactions.

4.2 Experimental Section

The presented four-port microfluidic device (Figure 18) addresses the specific mass-transport limitation of sample dispersion during convective transport in flow cell-based SPR detection platforms [176]. The device is particularly useful for small molecule kinetic measurements: rapidly switching between buffer and sample solutions on the order of milliseconds. This enables the detection of binding events that occur two orders of magnitude faster than the current limits of popular commercial SPR systems (Table 2) and expands the dynamic range of kinetic rate constant determination to values of $k_d < 130\ s^{-1}$ [150].

Figure 18. (a) Image of the four-port microfluidic device taken with an optical microscope using transmitted light. PDMS is cured on an SU-8 mold (60 µm height) fabricated using common soft lithography techniques. The device is press-clamped onto an Au sensor chip or permanently bound to a glass microscope slide with Au sensor regions using oxygen plasma. (b) Target receptors (e.g. IgG) are immobilized on an Au sensor surface prior to binding PDMS device. (c) A small Au sensor chip is fabricated on a glass microscope slide, allowing for a permanent bond between the PDMS device and the surrounding glass surface using oxygen plasma. Target receptors are bound to the surface using flow-based immobilization methods.

Table 2. Summary of the Kinetic Measurement Capabilities of Several Major Commercial SPR Platforms

		Measurement Limits		
Company	**Instrument**	**k_a [M^{-1} s^{-1}]**	**k_d [s^{-1}]**	**Sample Volume [µL]**
Biorad	ProteOn XPR 36	3×10^6	0.6	95
GE Healthcare	Biacore T200	5×10^7	1	22
	Biacore X100	1×10^7	0.1	20
	Biacore 3000	1×10^7	0.1	>21
	Biacore 4000	5×10^6	1	30
SensiQ Technologies	(All Products)	1×10^8	0.1	5
Plexara	PlexArray	1×10^6	.01	50
IBIS	IBIS-MX96	5×10^6	.05	*(n/a)*

Another advantage of this device is the minimal requirement of sample volume. Binding kinetics can be measured with as little as 1 µL of analyte solution, which enables measurement for precious samples.

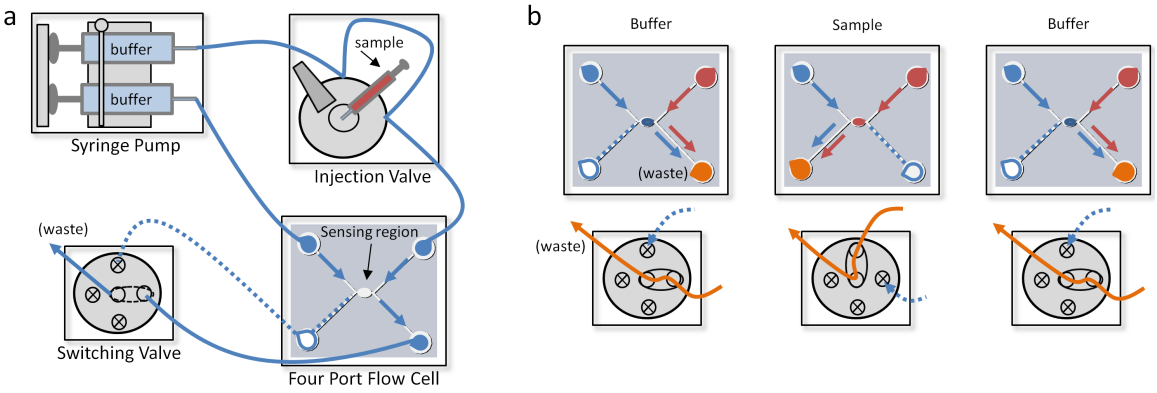

Figure 19. A schematic of the microfluidic delivery platform. (a) A syringe pump pushes buffer solution (blue) through the two inlet ports. One of the syringes is connected to an injection valve, allowing for the introduction of sample to the microfluidic device. The two outlet ports are connected to a high-speed switching valve. The switching valve allows for a single outlet port to flow at a time (open: solid line; closed: dotted line). By selecting which port is open, the direction of flow through the device and the composition of the solution (sample or buffer) in the central sensing area are controlled. (b) The relationship between the switching valve and the fluidic flow through the microfluidic device is illustrated. Buffer and sample (red) solutions flow through the device simultaneously, while only one solution flows over the central sensing area. The mixture (orange) of the solutions exits the device through the outlet port selected by the switching valve. The alternating opening and closing of the two outlets ports reverses the direction of flow and determines which solution flows over the central sensing area.

The four-port flow cell has two inlets and two outlets and is described in detail in Figure 19. Buffer flows into one inlet, and the sample flows into the other. The two outlets are

connected to a high-speed switching valve (Low Pressure Stream Selector Valve 1/16" and microelectric actuator, VICI Valco Instruments). Only one outlet is open at any given time, controlling the direction of flow through the microfluidic device and the composition of the solution localized to the sensor surface. Depending on which outlet is opened, the buffer or sample flows exclusively over the sensor surface, transitioning between the two rapidly. The small distance the sample travels to the sensing region minimizes the opportunity for sample dispersion (i.e. increased transition time). Note that the sample plug experiences dispersive effects due to diffusion of its constituent molecules as it travels from the injection valve to the microfluidic flow cell. However, the sample is not introduced to the sensing region of the flow cell until the switching valve selects the appropriate outlet port. The diffuse concentrations in the front and tail ends of the sample plug are never introduced to the sensing region, circumventing the dispersive effects of this initial travel time. The transition time will scale with the physical dimensions of the device and is inversely proportional to the fluid flow rate. At a volumetric flow rate of 5 μL/min, the devices pictured in Figure 18b and Figure 18c transitioned between buffer and sample in 26 ms and 7.6ms, respectively.

A two-dimensional computer simulation of the four-port microfluidic device was conducted using COMSOL's Convection & Diffusion in combination with the incompressible Navier-Stokes fluid dynamics application modes, and followed the assembly of the Fluid Valve (COMSOL Model ID: 315) [151]. The mass transport of 50 μM of a 100 Da molecule ($D = 4x10^{-10}$ m^2/s) with a constant influx rate of 5 μL/min was modeled using the physical dimensions of the device in Figure 18b. The simulated fluids were assumed to be Newtonian, and the default no-slip boundary conditions were employed. The alternate closing of the outlet ports was

modeled as local changes in fluid viscosity ($\mu \rightarrow \infty$). A summary of the simulated mass transport of the sample through the device is summarized in Figure 20a. Empirical measurement of the device's performance (170 mM ethanol in water, MW 46 Da, $D = 1.2x10^{-10}$ m^2/s) and the computed sample concentration profile at a central point (i.e. sensing region) in the flow cell device is plotted as a function of time in Figure 20b.

The device functionality was tested using a model IgG anti-IgG binding event on a homemade SPR platform. A non-contact piezoelectric inkjet printer (Engineering Arts LLC) was used to immobilize a uniform pattern of human IgG spots (via EDC/NHS coupling) with 200 μm spacing as previously described. Prior to the print, the Au sensor chip was functionalized with 5 mM of 50:1 PEG-OH:PEG-COOH in a 4:1 % v/v ethanol to water solution.

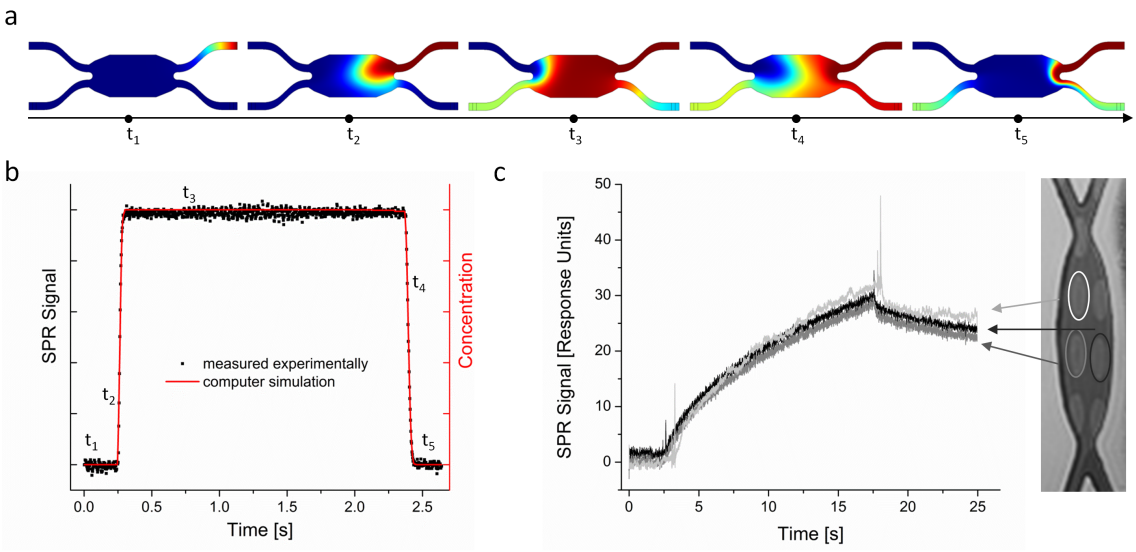

Figure 20. (a) COMSOL simulation of sample flow through four port flow cell. Buffer flow from the top left inlet and the sample solution flows from the top right inlet. The bottom two outlets are connected to a switching valve. The bottom left outlet is opened in the first three pictures, then is switched closed as the bottom right outlet is opened. The flow through the center sensing region reverses direction as the sample solution flows out the open outlet. (b) The sample concentration in the center sensor region of the flow cell is plotted in red as a function of time. The black scatter plot is experimental data showing the SPR sensor signal. The experimental data matches the COMSOL simulation almost exactly. (c) Experimental data showing an IgG/aIgG binding for three discrete printed spots.

1x PBS was used as a running buffer and filled the microfluidic device and tubing prior to the sample injection. A 1 µL sample solution of 20 µg/mL goat anti-human IgG was injected into the injection valve and allowed to run through the microfluidic device until the front edge of

the dispersed sample had passed through the microfluidic device, the sample was then introduced to the sensing region of the device for 20s then removed. Local areas on the sensor surface without immobilized IgG were used as reference regions. The reference-subtracted SPR sensorgrams for the binding event are shown in Figure 20c. The measured binding affinity (K_D = 22 nM) is consistent with values reported in the literature, while the measured association and dissociation rate constants (k_a = 1.069 x10^6 $M^{-1}s^{-1}$, k_d = 0.023 s^{-1}) are faster than expected [152]. This is due to the short recording time and single injection concentration. The high frame rate of the CCD camera (Pike, Allied Vision Technologies) rapidly fills the computer's memory buffer, setting an upper bound on the total recording time. Neither the association nor dissociation process was measured for a sufficiently long time to make an accurate measurement of the slow kinetics of this proof-of-principle binding event. These experimental artifacts are easily overcome and are irrelevant for the measurement of fast kinetic rate constants.

5. PLASMONIC-BASED ELECTROCHEMICAL IMPEDANCE MICROSCOPY

5.1 Introduction

The interactions between small molecules and biological macro-molecules constitute one of the most important components of biological networks. Communication between cells, expression of genes, and the entire immune system are dependent on a massively parallel network of binding interactions of proteins and small molecules. The development of drug candidates and the identification of biomarkers for clinical diagnosis rely on quick detection of target molecules in complex environments. Ideally, a detection technique provides information valuable kinetic information rigorous, quantitative measurements of binding events between small molecules and their biological receptors. Methods for elucidating these types of binding reactions are paramount for understanding of one the most fundamental mechanisms of biology.

Traditionally, it has been difficult to measure the binding affinities of small molecules. For most transducers, the signal is proportional to either the mass or concentration of the reactants. The diminutive size of small molecules presents an immediate obstacle in their detection. Many biologically-relevant small molecules are only available at low concentrations, further exacerbating the difficulties associated with small signal detection.

In 1977 the dependence of surface plasmon excitation on (interfacial) electron density was demonstrated for both gold and silver electrodes in contact with an electrolyte solution [153]. Twenty-three years later, Wang et al. demonstrated exquisite angular resolution of potential-modulated SPR measurement and laid the fundamental building blocks of Plasmonic-base Electrochemical Impedance Microscopy (P-EIM) [154]. Since then, the relationship between the electrical properties of an electrode sensor surface and the optical signal of conventional SPR has been explored.

The underlying principles governing surface impedance measurement were presented in a 2008 publication authored by Foley et al. [155]. In this work, Foley et al. demonstrate surface impedance imaging and extract local amplitude and phase information from sensor surface. A gold sensor electrode was partially patterned with 1-dodecanethiol (DDT) and examined via conventional and the novel Surface Impedance Imaging Technique. The two measured values were found to be in close agreement, and a theoretical framework for interpreting the real and imaginary parts of the ac SPR signal were formulated (more below).

A number of electrochemical measurements have been conducted capitalizing on the fundamental dependence of SPR on surface charge density. Wang et al. developed a quantitative formalism of electrochemical surface plasmon resonance (EC-SPR) [156]. EC-SPR was shown to have several unique advantages over conventional convolution voltammetry, including high spatial resolution and surface sensitivity. Huang et al. exploited the spatial resolution of this technique by simulataneously monitoring the electrochemical current and conventional SPR signals of several stages of the hydroquinone-benzoquinone (HQ-BQ) reaction system [157]. Using EC-SPR they were able to monitor the kinetics and identified the semiquinone radical anion as an intermediary phase of the HQ-BQ reaction. Shan et al. explored the relationship between SPR and surface charge density via the response of particles to various surface chemistries [158] and to ac potentials applied to a sensor surface [159].

5.2 Theory of P-EIM

The following discussion follows the methodology as reported by Foley et al. The SPR resonance angle θ_R is a function of the dielectric constant of the metal film ε_m as defined by:

$$\sin(\theta_R) = \sqrt{\frac{\varepsilon_1 \varepsilon_m}{(\varepsilon_1 + \varepsilon_m)\varepsilon_2}} \tag{41}$$

where ε_1 and ε_2 are the dielectric constants of the buffer solution and prism, respectively. According to the Drue model, ε_m is a function of frequency:

$$\varepsilon_m(f) = 1 - \frac{n_e \mathrm{e}^2}{\varepsilon_0 m_e 4\pi^2 f^2} \tag{42}$$

where e, m_e, and n_e are the electron charge, mass, and density, respectively, and $\varepsilon_m = 8.85\times10^{-12}$ F/m. For a thin metal film of thickness d_m, the relationship between electron density and the surface charge $\Delta\sigma$ can be written as:

$$\Delta\sigma = -e d_m \Delta n_e \tag{43}$$

Changes in the surface charge density may thus be written as:

$$\Delta\sigma = -\frac{e d_m \Delta n_e}{\varepsilon_m - 1}\Delta\varepsilon_m \tag{44}$$

The relationship between the resonance angle shift and changes in surface charge density is given by:

$$\Delta\sigma = \alpha \Delta\theta_R \tag{45}$$

where

$$\alpha = -\frac{e d_m \Delta n_e \varepsilon_2 (\varepsilon_1 + \varepsilon_m)^2 \sin(2\theta_R)}{\varepsilon_1^2(\varepsilon_m - 1)} \tag{46}$$

Foley et al. allow that Drude model provides a semi-quantitative description of their empirical data, and expect that α will be refined as a more sophisticated model is developed. The interfacial capacitance density c is related to surface charge density by:

$$\Delta\sigma = c\Delta V_{int} \tag{47}$$

where ΔV_{int} is the fraction of applied voltage dropped across the electrode/solution interface. Therefore, the interfacial capacitance of a sensor surface can manifest in an optical SPR signal:

$$c(x,y) = \alpha \Delta\theta_R(x,y)/\Delta \mathrm{V} \tag{48}$$

Foley et al. use a Randles equivalent circuit (Figure 21) to model the electrochemical setup: the electrolyte solution is understood to have a resistance R_s, and the metal-solution interface is modeled as a capacitor (C_p) and resistor (R_p) in parallel.

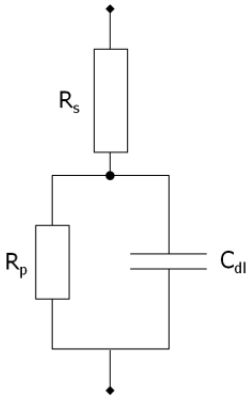

Figure 21. Randles equivalent circuit for P-EIM

The fraction of applied voltage dropped across the solution versus the fraction dropped across the electrode/solution interface is determined by their respective impedance values:

$$Z_{tot}(x,y) = Z_s + Z_p(x,y) = R_s + \frac{1}{\frac{1}{R_p} + j\omega C_p(x,y)} \tag{49}$$

where C_p is the total capacitance of the metal-solution interface and is a function of position (x,y). The potential drop across the interface ΔV_{int} is related to the applied potential ΔV_{app} as described by:

$$\Delta V_{int}(x,y) = \frac{Z_p(x,y)}{Z_{tot}(x,y)} \Delta V_{app} \tag{50}$$

The local resonance angle is expressed as:

$$\Delta\theta_R(x,y) = \frac{C_p(x,y)}{\alpha} \frac{Z_p(x,y)}{Z_{tot}(x,y)} \Delta V_{app} \tag{51}$$

In the absence of electrochemical reactions on the electrode, the surface resistance R_p may be modeled as infinite. The relationship between the resonance angle and applied voltage may be rewritten as:

$$\frac{\Delta\theta_R(x,y)}{\Delta V_{app}} = \frac{C_p(x,y)}{\alpha} \frac{1}{j\omega C_p(x,y)} \frac{1}{Z_{tot}(x,y)} = \frac{1}{j\omega\alpha Z_{tot}(x,y)} \tag{52}$$

Note that the observed SPR signal contains information of the total impedance of the electrode and solution system; this impedance has both real and imaginary parts (or equivalently, amplitude and phase information). Reducing the resistance of the electrolyte solution further reduces the above equation to:

$$\frac{\Delta\theta_R(x,y)}{\Delta V_{app}} = \frac{C_p(x,y)}{\alpha} \tag{53}$$

5.3 Data

5.3.1 Summary

Charge-based detection of small molecules is demonstrated by plasmonic-based electrochemical impedance microscopy (P-EIM) [175]. The dependence of surface plasmon resonance (SPR) on surface charge density is used to detect small molecules (60-120 Da) printed on a dextran-modified sensor surface. Local variations in charge density on an electrode surface are manifest in an optical SPR signal. The SPR response to an applied ac potential measures the

sensor surface impedance, which is a function of the surface charge density. This optical signal is comprised of a dc and an ac component, and is measured with high spatial resolution. The dc element of the SPR signal represents conventional SPR imaging information. The amplitude and phase of local surface impedance is provided by the ac component. The phase signal of the small molecules is a function of their charge status, which is manipulated by the pH of a solution. Small molecules with positive, neutral, and negative charge are detected by P-EIM. This technique is used to detect and distinguish small molecules based on their charge status, thereby circumventing the mass limitation (~100 Da) of conventional SPR measurement.

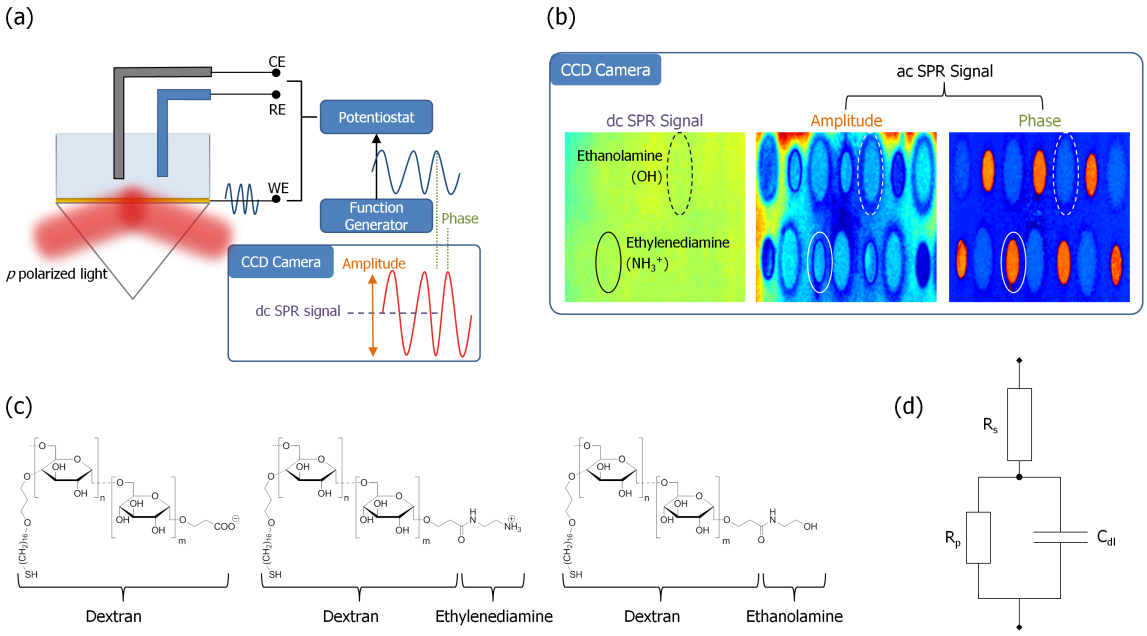

Figure 22. (a) Schematic illustration of the P-EIM setup. An ac potential modulation from a function generator is applied to the Au sensor chip (WE) via a potentiostat. (b) The P-EIM signals of printed small molecules spots (ethylenediamine and ethanolamine conjugated to dextran surface via EDC/NHS coupling chemistry, indicated by solid and dash circles, respectively) are imaged by a CCD camera, and vary with the applied voltage. The dc component of the response is the average intensity, and the ac component is comprised of a phase (relative to the applied potential) and amplitude (peak-to-peak amplitude). (c) Molecular structures of the charged dextran/small molecule conjugates. (d) The Randles equivalent circuit is used to model the electrical response of the sensor chip. The solution has a resistive effect (R_s), and the double layer formed on the interface between the sensor surface and solution (where the small molecules bound to) has both resistive (R_p) and capacitive (C_{dl}) characteristics [175].

5.3.2 Introduction

The interactions between small molecules and biological macro-molecules constitute a crucial component of biological networks and are the subject of extensive investigation in both academic and commercial laboratories. Important biological processes such as communication between cells, expression of genes, and immune response are dependent on massively parallel networks of the transient interactions of proteins and small molecules. Drug discovery and biomarker validation for clinical diagnosis rely on rigorous, quantitative measurements of binding events between small molecules and their biological receptors [160]; small molecules (generally <1000 Da) currently represent over 90% of FDA approved drugs [161]. The development of detection techniques for elucidating these types of binding reactions is paramount for the advancement of pharmacology and health therapeutics.

Current techniques to measure small molecule binding kinetics employ labels to detect the small molecule or its bound target, or alternatively, measure an intrinsic characteristic of the binding event or its constituent molecules in a "label-free" detection platform [162-165]. The decision to use a particular measurement technique is informed by its inherent strengths and weaknesses, and the specific requirements for the intended measurement (e.g. sensitivity, selectivity, throughput, etc.). For example, the use of labels to enhance measurement sensitivity must be weighed against the potential consequence of adversely affecting the system being measured [166, 167]. By definition, label-free methods eschew this risk but may suffer from other limitations such as weak signals and non-specific binding [168].

The potential of plasmonic-based impedance imaging techniques for studying the binding of macro-molecules including antigen/antibody binding events has been previously demonstrated

[155, 156, 169-171]. In a recent demonstration the real-time electrical impedance signal followed the kinetics of the protein association and dissociation process and was less prone to the various sources of noise in conventional SPR measurements (i.e. bulk refractive index changes, non-specific adsorption) [172].

Here is presented a novel label-free technique for detecting and imaging small molecules using plasmonic-based electro-chemical impedance microscopy (P-EIM). The molecules' charge is expressed in the phase component of the electro-chemical impedance, and therefore small molecules with charge different than the substrate can be detected with distinct phase signals. In addition, charge status of small molecules and/or the substrate can be manipulated by changing solution pH, and therefore in principle, any small molecules can be detected regardless the charge status and mass of molecules

P-EIM may be immediately useful for a variety of applications. It could be used to directly measure small molecule binding events that have traditionally generated too small a signal for high throughput label-free assays (e.g. drug discovery). The study of post-translational modification (PTM) is another potential application of P-EIM: for example, monitoring the change in charge status due to the addition of charged phosphate groups during a phosphorylation event [173].

5.3.3 Materials

16-mercaptohexadecan-1-01, epichlorohydrin, diethylene glycol dimethyl ether (diglyme), dextran, bromoacetic acid, N-(3-dimethylaminopropyl)-N'-ethylcarbodiimide hydrochloride (EDC), ethanol, ethanolamine, ethylenediamine dihydrochloride (ethylenediamine), $NaOH$, H_2SO_4, and Na_2CO_3, were purchased from Sigma (St. Louis, MO).

5.3.4 Chip Preparation

The Au sensor chips were rinsed with water and ethanol then annealed with hydrogen flame. The chips were treated with 5 x 10^{-3} M solution of 16-mercaptohexadecan-1-01 in a 4:1 ethanol to water solution overnight at 25 °C. The resulting hydrophilic surfaces were then reacted with 0.6 M solution of epichlorohydrin in a 1:1 mixture of 0.4 M sodium hydroxide and diglyme for 4 hours at 25 °C. After thoroughly washing with water, ethanol, and water again, the chips were treated with a basic dextran solution (3 g dextran in 10 mL of 0.1 M sodium hydroxide) for 20 hours at 25 °C. Further functionalization of the carboxymethyl-modified matrix was done by reaction with bromoacetic acid (1 M solution in 2 M sodium hydroxide) for 20 hours at 25 °C. The dextran-modified sensor chips were rinsed with water, dried with nitrogen gas, and stored at 4 °C under nitrogen gas.

5.3.5 Small Molecule Printing

1 M stock solutions of water mixed with ethylenediamine and ethanolamine, respectively, were prepared preceding the print. Both of these small molecules have at least one amine group, which is used for their immobilization to the dextran surface via EDC coupling. 20 µL of each solution was mixed with 20 µL 0.8 M EDC in water immediately prior to printing. The solutions were deposited at discrete spots on the dextran modified gold surfaces. A non-contact piezoelectric inkjet printer (Engineering Arts LLC) was used to deposit a uniform pattern of spots with 500 µm spacing. A short, 22.5 KHz, burst of 5 drops deposited ~0.5 nL of solution at each spot. Precise dew-point control was used during printing to mitigate evaporation of the spots. Relative humidity (65%) and temperature (24 °C) were precisely regulated inside the printing chamber. The gold surfaces were chilled to 21 °C which is a few degrees above the

dew-point temperature (17 °C) to prevent condensation. After printing, the gold surfaces were maintained with dew-point control for 50 minutes and then stored under argon gas at 4 °C. Two batches of two chips were prepared to mitigate any variability transmitted from unknown nuisance factors of the printing process.

The printed spots on the sensor surface represent areas of high small molecule concentration (Figure 25). The P-EIM signals from these regions of interest (ROIs) are determined by the intrinsic properties of the small molecules (i.e. charge status) and environmental factors such as their distributions of mass from the printing process. Additionally, as the small molecules are immobilized in a three dimensional hydrogel, the underlying dextran infrastructure also influences their P-EIM responses. These spots are prudently referred to as ROIs to reflect the ambiguity of their local print density and distribution.

5.3.6 Plasmonic Based Impedance Measurements

A custom SPR measurement system based on the Kretschmann configuration was used for the following experiments. A temperature-controlled (TCLDM9, ThorLabs) LED (wave-length 670 nm, Hamamatsu) was used as a light source. Reflected light from a BK7 triangular prism was collected by a CCD camera (Pike, Allied Vision Technologies) with a 2.5-10X variable magnification lens (Edmund Optics). The SPR sensor chips (44 nm gold on a 1.5 nm chromium layer) were fabricated by thermal evaporation at high vacuum (3×10^{-6} Torr) on BK7 glass cover slides. Four Au chips were prepared in two batches to block any unknown effects of chip fabrication. The Au sensor chip served as a working electrode (WE) while silver and platinum wires were used as reference (RE) and counter electrodes (CE), respectively Figure 22a). A potentiostat (EG&G model 283 potentiostat/galvanostat, Princeton Applied Research)

controlled the potential of the WE with respect to the CE. A 10 s ac potential modulation of 500 mV (dc offset of 100 mV) at a frequency of 10 Hz was applied to the sensor chip for each solution pH, and was controlled by an external function generator (model 33521A, Agilent). A PDMS gasket placed on top of the sensor surface formed an open well to house the solution and electrodes.

The pH of the solution was used to control the charge status of the printed small molecules and dextran surface. Three solutions were prepared at 0.5 mM: H_2SO_4 (pH 1), NaOH (pH 5) and Na_2CO_3 (pH 9). A low ionic strength is used to reduce the charge-screening effect of an electric double layer [158]. The solution was removed via pipette prior to the addition of a subsequent solution. All three buffers were used for each of the four chips tested, and the run order of the buffer pH was randomized. The selection of the applied voltage amplitude, frequency, and offset potential were controlled via homemade Matlab software. The camera output and potential modulation signals were captured by a data acquisition board (NI USB-6251, National Instruments) using the same Matlab program. A fast Fourier transform algorithm was applied to the SPR image data captured by the CCD camera to generate phase and amplitude information for the imaged sensor surface.

5.3.7 Basic Principle and Set-up

Conventional electrical impedance spectroscopy measures the electrical current response (ΔI) of an electrode surface to an applied ac potential modulation (amplitude ΔV applied at frequency ω) to determine surface impedance ($Z(\omega) = \Delta V/\Delta I$). In contrast, P-EIM does not require electrical current measurement; the principle of P-EIM is based on the dependence of the SPR signal ($\Delta\theta$) on the surface charge density ($\Delta\sigma$) of the sensor. The NJ Tao laboratory has

previously shown that $\Delta\theta$ is proportional to $\Delta\sigma$, given by $\Delta\sigma = \alpha\Delta\theta$, where α is a coefficient that can be calibrated experimentally or calculated theoretically[8]. The current density (ΔJ) on the sensor surface is related to charge density by $\Delta J = j\omega\Delta\sigma$ (where $j = \sqrt{-1}$). Therefore, the local surface impedance density can be determined by the ac component of the SPR signal ($\Delta\theta$) as given by $Z(\omega) = j\omega\alpha\Delta\theta/\Delta V$.

The measured response of the P-EIM technique is simply an optical signal of light intensity, varying sinusodially with time due to the modulation of applied electrical potential. The dc component is the average intensity of this signal and represents conventional SPR measurement; it is a function of the local refractive index on, and immediately above, the sensor surface. The ac signal has an amplitude and phase (or equivalently, real and imaginary parts), which represent the electrochemical impedance density on the sensor surface. The dc and ac SPR signals are simultaneously measured to provide high resolution SPR imaging and electrochemical impedance imaging capabilities in the same setup.

5.3.8 Effect of Solution pH

The charge status of a small molecule ROI is determined by the protonation status of the immobilized molecules' terminal functional groups, which is a function of the pH of the solution (Table 3). The respective pK_A values of ethylenediamine and ethanolamine were determined from the Curtipot program [174]. The unbound end of the printed ethanolamine regions are terminated with OH functional groups and remain neutral in the pH range of the tested solutions. At a pH below 3.5, the dextran surface does not carry a charge; the COOH terminal groups remain neutral[11]. The unbound end of the immobilized ethylenediamine is terminated with one amine group, which carries at positive charge (NH_3^+) at the low solution pH. As the pH of the

solution increases, the terminal groups on the dextran surface become negatively charged (COO^-). The positively charged amine groups are neutral (NH_2) at pH 9 and the ethylenediamine ROIs lose their positive charge.

Table 3. Charge Status of Small Molecule Terminal Groups as a Function of Solution pH

	Solution pH		
Molecule	1	5	9
Ethanolamine	OH	OH	OH
Dextran	$COOH$	COO^-	COO^-
Ethylenediamine	NH_3^+	NH_3^+	NH_2

5.3.9 Impedance Models

The impedance response of the sensor can be described by an electrical model using a Randles equivalent circuit and a mechanical model of the three-dimensional dextran hydrogel response (Figure 22d, Figure 23, Figure 24). The solution is understood to have a resistive effect (R_s), and the double layer formed on the interface between the sensor surface and solution has both resistive (R_p) and capacitive (C_{dl}) characteristics. The NJ Tao laboratory has previously derived the relationships of these three electrical components and I only list their final form here[9]. According to the model, the current amplitude and phase on the sensor surface is given by:

$$I_{amp} = \left| \frac{\Delta V}{R_s + \left(R_p^{-1} + j\omega C_{dl}\right)^{-1}} \right| \tag{54}$$

$$I_{phase} = Arg\left(\frac{\Delta V}{R_s + \left(R_p^{-1} + j\omega C_{dl}\right)^{-1}} \right) \tag{55}$$

The modification of the sensor surface with a flexible dextran hydrogel adds an additional layer of complexity to the impedance model, as the hydrogel responds mechanically to the driving force of the ac potential. This response to the applied potential can be modeled as a driven harmonic oscillator with a spring constant that changes as a function of charge density.

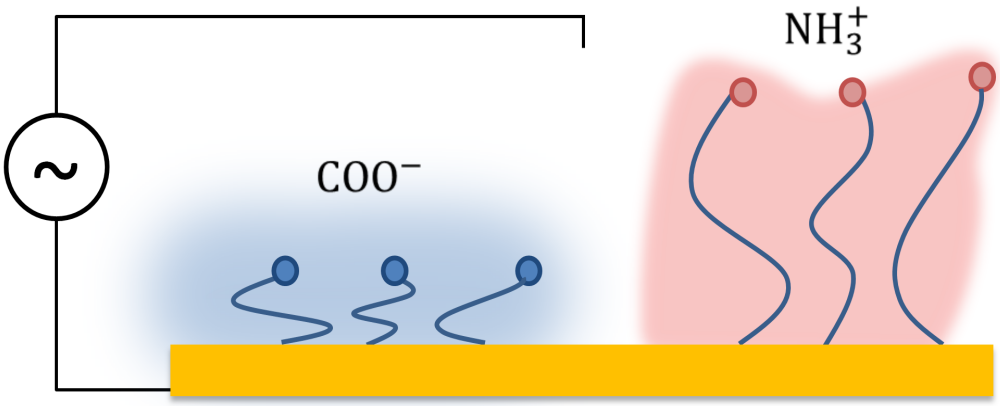

Figure 23. Illustration of the mechanical response of the dextran surface (blue lines). The solution pH determines the charge status of the terminal groups (dots). In general, the presence of charge increases the force from the applied potential on by the dextran surface, resulting in greater amplitudes of fluctuation. Regions with positive charge respond 180° out of phase relative to negatively charged ROIs.

The mechanical response of the dextran hydrogel on the sensor surface can be modeled as a viscoelastic medium driven by the force from the applied potential ($\vec{F} = \pm q\vec{E}$); the charged functional groups of the hydrogel and small molecule ROIs are displaced ($x = x_0 e^{-j\omega t}$) by the

electric field according to the polarity of their charge (Figure 23). The mechanical response of the flexible hydrogel layer to the electrostatic driving force is described by k, the elastic restoring force constant, and g, the internal damping of the polymer matrix. The corresponding equation takes the form of:

$$j\omega x_0 e^{-j\omega t} + k x_0 e^{-j\omega t} = \pm q\vec{E} \tag{56}$$

The displacement of a local region on the surface is described by:

$$x = \frac{\pm q\vec{E}}{\gamma j\omega + k} \tag{57}$$

Regions with a high density of charge experience an additional repulsive force between similarly-charged functional groups, causing the hydrogel to become more rigid (Figure 24). This rigidity is the equivalent of a change in k.

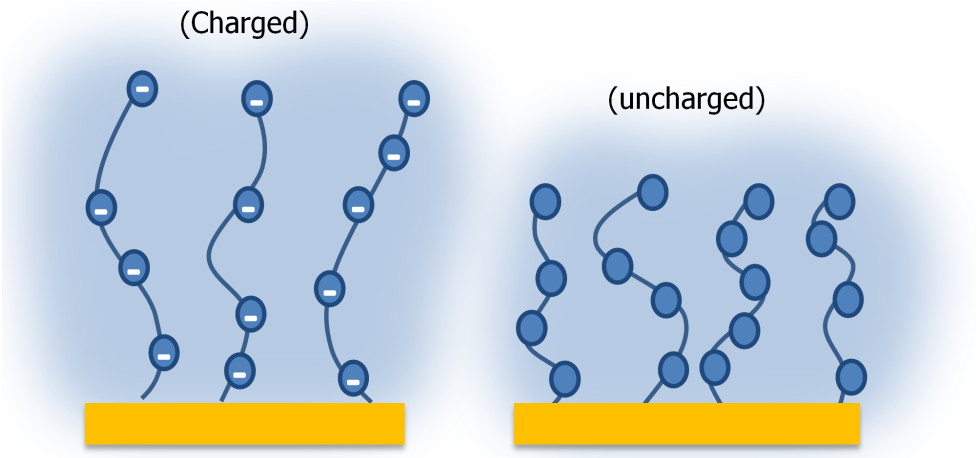

Figure 24. The repulsive electrical force between the charged terminal groups causes the dextran to expand (left). Dextran is more rigid in this state, decreasing the amplitude of SPR fluctuation. However, the presence of charge allows the hydrogel to respond to the driving ac potential, possibly increasing its amplitude of SPR fluctuation.

The parameters in the Randles model are related to the viscoelastic model, but an explicit expression requires further information and assumptions. For example, the small molecules are not immobilized with a 100% printing efficiency; not every dextran terminal group in a small molecule ROI is used to bind the small molecule. The impedance response of the small molecule ROIs are influenced by these un-coupled carboxyl groups. Quantitative analysis of the absolute impedance signal is thus difficult but fortunately unnecessary for the purposes of small molecule detection. Instead, consider the relative differences in impedance response between the different small molecule ROIs and dextran background. Due to the convolution of effects outlined above, the phase component of the impedance signal is examined, which follows the simple model of charge-based response.

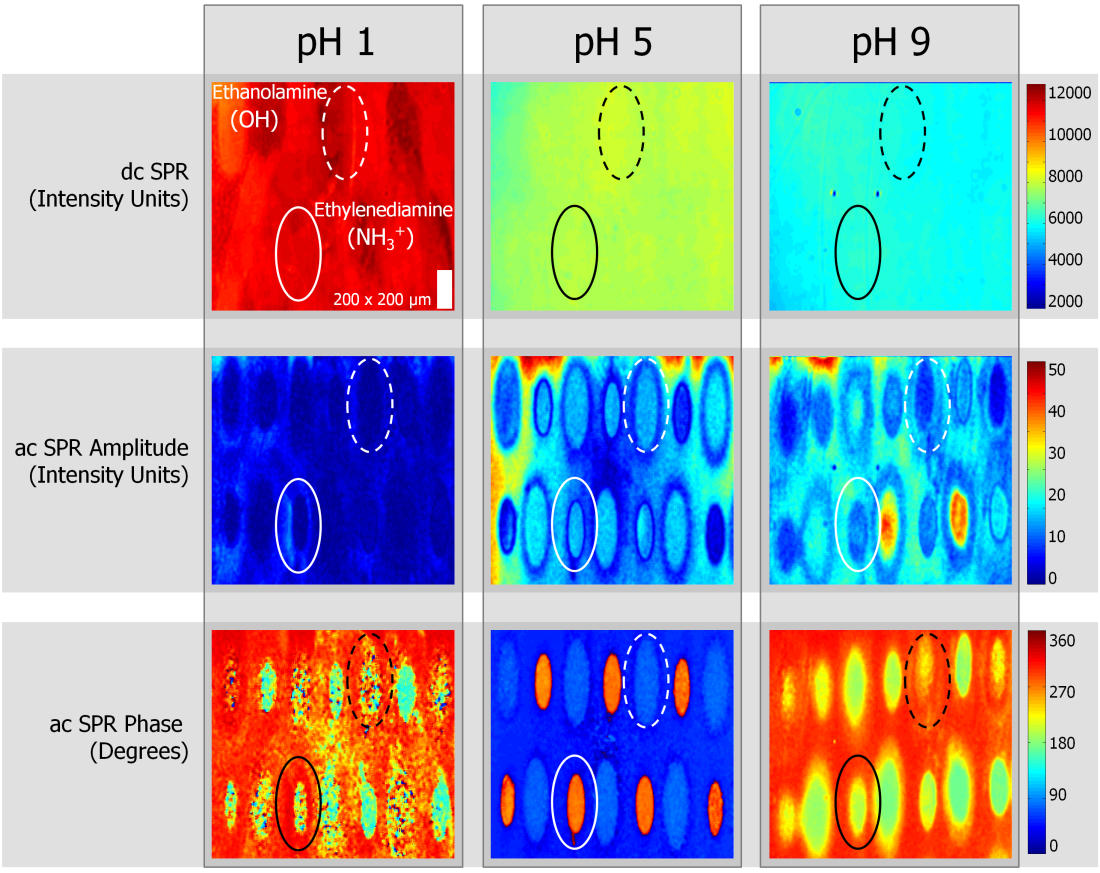

Figure 25. Dc and ac SPR signals as a function of solution pH. Ethanolamine and ethylenediamine are printed in an alternating pattern with 500 µm spacing on a dextran-functionalized Au microscope slide. (Top) The masses of the immobilized ethanolamine and ethylene small molecules are too small (60-120 Da) to be detected by conventional dc SPR. (Middle) The amplitude component of the ac SPR signal reveals the presence of the small molecules, but does not differentiate between them in an obvious manner. (Bottom) The phase component clearly distinguishes the small molecules based on their charge status. At pH 1 the neutrally charged COOH terminal groups of the dextran background are 90° out of phase from the positively charged NH_3^+ terminal groups of the ethylenediamine regions of interest (ROIs). The neutrally charged ethanolamine ROIs (OH) are also resolved but have a larger distribution of

phase response. At pH 5 the dextran is negatively charged (COO^-) and is 180° out of phase with the positively charged ethylenediamine ROIs. At pH 9 the ethylenediamine ROIs become neutral and the phase contrast between the neutral and charged ROIs returns to 90°.

5.3.10 Amplitude Component

At pH > 3.5, the terminal groups of the dextran hydrogel have a net negative charge. These localized charges repel each other and cause the dextran to expand above the sensor surface. The reorganization of mass away from the sensor surface is confirmed by the decreased dc SPR signal at high pH (Figure 25). In this charged state the dextran surface is rigid and resists modulation by the applied potential. As explained above, the presence of charge has the additional effect of increasing the mechanical dextran response to the applied potential, which theoretically increases the amplitude of its fluctuation. As the number of negatively charged terminal groups increases, the hydrogel experiences a larger force from the applied potential and the dextran impedance decreases. At low pH the impedance-damping effect of rigidity is reduced but the uncharged dextran matrix experiences a smaller force from the applied voltage. The relationship between these two competing forces obfuscates the net impedance response of dextran and does not allow for an unambiguous interpretation of the amplitude component of the P-EIM signal.

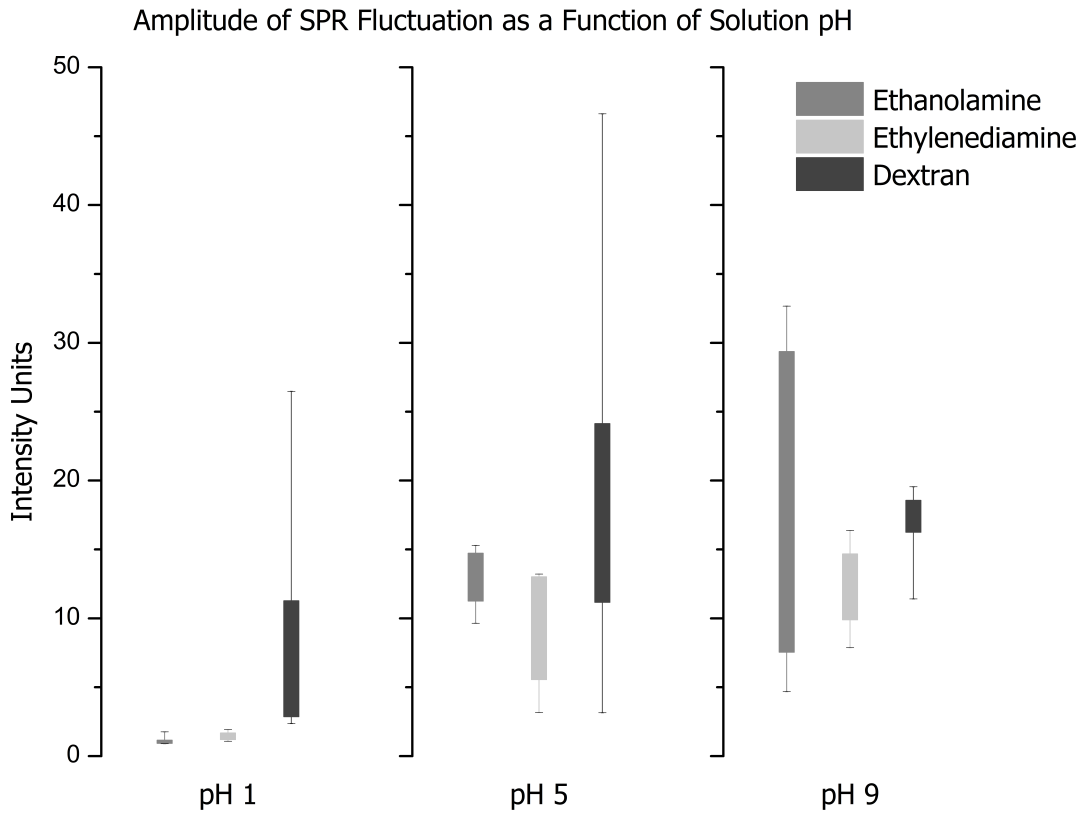

Figure 26. Box plots of pixel intensity of small molecule and dextran ROIs in the P-EIM amplitude images (filled boxes represent 25%-75% of mean values, minimum and maximum values marked by whiskers). The amplitude component of the P-EIM signal does not demonstrate any obvious patterns of SPR fluctuation for the small molecules or dextran ROIs.

Note that the presence of the small molecules (undetected by the conventional SPR signal) is easily confirmed by their amplitude signals (Figure 25, Figure 26). However, the phase responses of differently-charged small molecules are much clearer, and allow for distinction based on charge status.

5.3.11 Phase Component

A small molecule ROI's phase response is a function of its charge status and environmental effects such as the response of the underlying dextran matrix. The determination of the absolute phase signal is confounded by the multi-variable response of the dextran hydrogel, and ultimately unnecessary. In the presence of an ac electric field, positively charged regions will respond up to 180° out of phase with negatively charged regions according to the oscillator model. The relative phase contrast of the differently charged regions is sufficient to detect and identify the small molecules.

At low pH, the positively charged ethylenediamine ROIs respond approximately 90° out of phase relative to the neutral ethanolamine and dextran regions. At pH 5, the positively charged ethylenediamine ROIs are 180° out of phase with the negatively charged dextran matrix. When the ethylenediamine regions lose their positive charge at high pH, the phase contrast between the neutral and negatively charged regions decreases to 90°. These results are summarized in Figure 27.

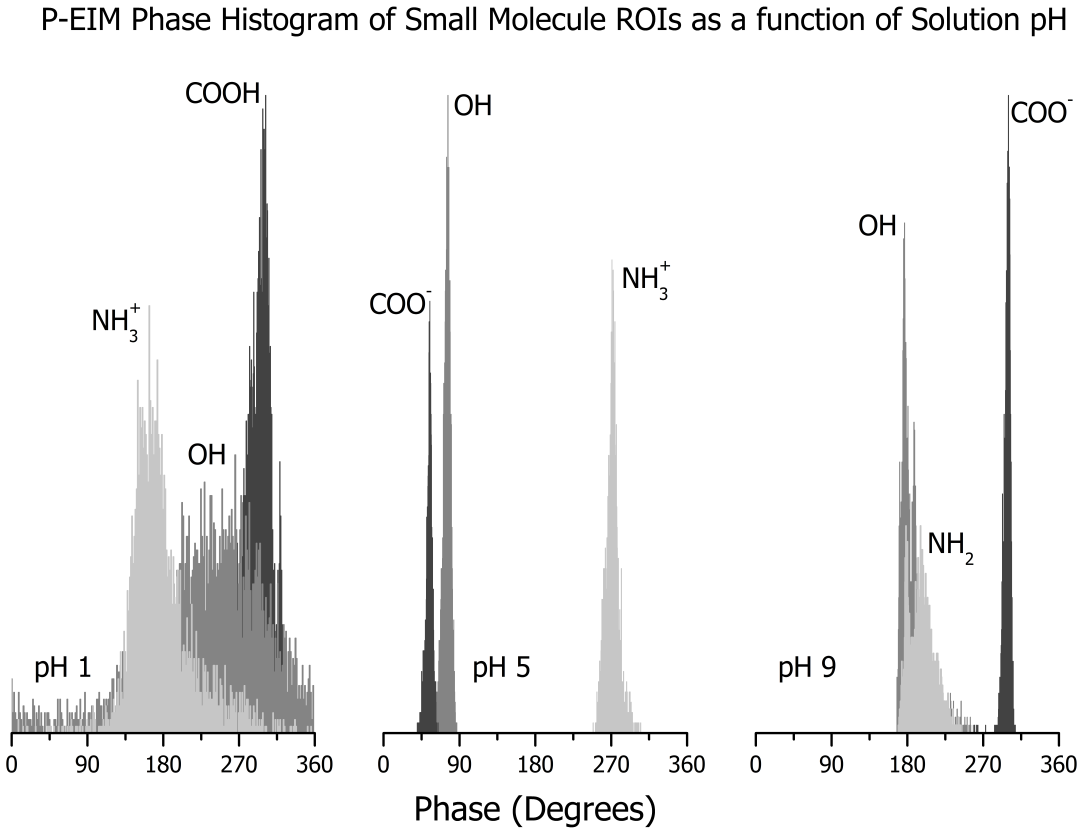

Figure 27. Pixel intensity histograms of small molecule and dextran ROIs in the P-EIM phase images. The P-EIM phase signal allows for the detection and identification of small molecules based on their charge status. At a solution of pH 1, regions with immobilized ethylenediamine (NH_3^+ functional groups) are approximately 90° out of phase with neutrally charged dextran (COOH) and ethanolamine (OH) ROIs. When the solution pH is increased above the pK_A of the dextran surface to pH 5, there is a 180° phase contrast between the positively charged functional groups of the ethylenediamine and the negatively charged carboxyl groups of dextran. At pH 9 the ethylenediamine functional groups lose their positive charge and are once again 90 ° out of phase with the negatively charged dextran ROIs.

Ideally, the neutral charge status of the ethanolamine ROIs would remain unchanged as a function of solution pH. However, this would require a 100% printing efficiency in which every terminal group of the dextran matrix binds to an ethanolamine small molecule during the printing process. It is reasonable to assume that the not every dextran terminal group is consumed during the print in the ethanolamine ROIs and that the remaining unmodified COOH regions follow the general trend of the global dextran matrix. The histogram plots of the ethanolamine regions tend to follow the dextran response, but their phase response never exceeds that of the dextran. The influence of the unmodified dextran terminal groups is greater in the neutrally-charged ethanolamine than the ethylenediamine ROIs (which have positively charged terminal groups to screen the surrounding negative charge and present a net positive charge).

5.4 Conclusion

Charge-based detection of small molecules is demonstrated using plasmonic-based electrochemical impedance microscopy (P-EIM). The P-EIM phase signal was found to be a function of localized surface charge; the phase contrast between differently-charged printed small molecules and a dextran hydrogel sensor surface was used to detect and identify the small molecules, and was validated by the pH dependence of the various ROIs' charge statuses. The technique requires that a small molecule target be differently charged than the binding or background surface, which can be achieved by control of solution pH and/or selection of proper probing/referencing molecules. Therefore this technique is applicable to small molecules with any charge status. More importantly, this "proof-of-principle" P-EIM measurement provides a

mass independent signal that could potentially be used to measure post-translational modifications or small molecule binding events in drug discovery or clinical diagnostics.

REFERENCES

[1] National Center for Biotechnology Information. <http://www.ncbi.nlm.nih.gov> (accessed in September 2013).

[2] Schilstra MJ and Martin SR. Methods in Enzymology, 467 (2009), 381-409.

[3] Comess KM, Schurdak ME. Current Opinions in Drug Discovery Development, 7 (2004), 411-416.

[4] Fandrich M, Tito MA, Leroux MR, Rostom AA, Hartl FU, Dobson CM, Robinson CV. Proceedings of the National Academy of Science U.S.A, 97 (2000), 14151–14155.

[5] Cheng XH, Gao QY, Smith RD, Jung KE, Switzer C. Chemistry Communications, (1996), 747–748.

[6] Jørgensen TJD, Staroske T, Roepstorff P, Williams DH, Heck AJR. Journal of the Chemical Society, Perkin Transactions 1, 2 (1999), 1859–1863.

[7] Kempen EC, Brodbelt JS. Analytical Chemistry, 72 (2000), 5411-5416.

[8] Greig MJ, Gasu HJ, Cummins LL, Sasmor H, Griffey RH. Journal of the American Chemical Society, 117 (1995), 10765-10766.

[9] Eckhart K, Spiess J. Journal of the American Society of Mass Spectrometry, 6 (1995), 912-919.

[10] Yamashita M and Fenn JB. Journal of Physical Chemistry, 88 (1984), 4671.

[11] Karas M, Bachman D, Bahr U, Hillenkamp F. International Journal of Mass Spectrometry and Ion Processes, 78 (1987), 53–68.

[12] Tanaka K, Waki H, Ido Y, Akita S, Yoshida Y, Yoshida T. Rapid Communications Mass Spectrometry, 20 (1988), 151–153.

[13] Cohen LH, Gusev AI. Analytical and Bioanalytical Chemistry, 373 (2002), 571-586.

[14] McCombie G, Knochenmuss R. Analytical Chemistry, 76 (2004), 4990-4997.

[15] Daniel J, McCombie G, Wednt S, Zenobi R. American Society for Mass Spectrometry, 14 (2003), 442-448.

[16] Heck AJR, van den Heuvel RHH. Mass Spectrometry Review, 23 (2004), 368-389.

[17] Sharon M, Robinson CV. Annual Review of Biochemistry, 76 (2007), 167-193.

[18] Kitova EN, Soya N, Klassen JS. Analytical Chemistry, 83 (2011), 5160-5167.

[19] Siegel MM, Tabei K, Bebernitz GA, Baum EZ. Journal of Mass Spectrometry, 33 (1998), 264-273.

[20] Kelly MA, McLellan TJ, Rosner PJ. Analytical Chemistry, 74 (2002), 1-9.

[21] Zhao YZ, van Breeman RB, Nikolic D, Huang CR, Woodbury CP, Schilling A, Venton DL. Journal of Medicinal Chemistry, 40 (1997), 4006-4012.

[22] Ng ESM, Yang F, Kameyama A, Palcic MM, Hindsgaul O, Schriemer DC. Analytical Chemistry, 77 (2005), 6125-6133.

[23] Annis DA, Athanasopoulos J, Curran PJ, Felsch JS, Kalghatgi K, Lee WH, Nash HM, Orminati JP, Rosner KE, Shipps GW Jr, Thaddupathy GRA, Tyler AN, Vilenchik L, Wagner CR, Wintner EA. International Journal of Mass Spectrometry, 238 (2004), 77-83.

[24] McGovern SL, Caselli E, Grigorieff N, Shoichet BK. Journal of Medicinal Chemistry, 45 (2002), 1712.

[25] Johnson BM, Nikolic D, van Breemen RB. Mass Spectrometry Reviews, 21 (2002), 76-86.

[26] Chen CJ, Chen S, Woodbury CP, Venton DL. Analytical Biochemistry, 261 (1998), 164-182.

[27] Schriemer DC, Bundle DR, Li L, Hindsgaul O. Angewante Chemistry International Edition, 37 (1998), 3383-3387.

[28] Kasai K, Ishii S. Journal of Biochemistry, 14 (1975), 261-264.

[29] Schriemer DC. Analytical Chemistry, 76 (2004), 440A-448A.

[30] Sharma J, Besanger TR, Brennan JD. Analytical Chemistry, 80 (2008), 3213-3220.

[31] Varenne A, Gareil P, Colliec-Jouault S, Daniel R. Analytical Biochemistry, 315 (2003), 152-159.

[32] Zavaleta J, Chinchilla D, Brown A, Ramirez A, Calderon V, Sogomonyan T, Gomez F. Current Analytical Chemistry, 2 (2006), 35-42.

[33] Lewis LM, Engle LJ, Pierceall WE, Hughes DE, Shaw KJ. Journal of Biomolecular Screening, 9 (2004), 303-340.

[34] Geoghegan KF and Kelly M. Mass Spectrometry Reviews, 24 (2005), 347-366.

[35] Muckenschnabel I, Falchetto R, Mayr LM, Filipuzzi I. Analytical Biochemistry, 324 (2004), 241-249.

[36] Zhang B, Palcic MM, Schriemer DC, Alvarez-Manilla G, Pierce M, Hindsgaul O. Analytical Biochemistry, 299 (2001), 173-182.

[37] Van Weemen BK, Schurrs AHWM. FEBS Letters, 15 (1971), 232-236.

[38] Engvall E, Perlmann P. Immunochemistry, 8 (1971), 871-874.

[39] Yallow RS, Berson SA. Clinical Investigations, 39 (1960), 1157-1175.

[40] Bock JL. American Journal of Clinical Pathology, 113 (2000), 628-646.

[41] Nam JM, Thaxton, CS, Mirkin CA. Science, 301 (2003), 1884–1886.

[42] Heath JR, Davis MR. Annual Review of Medicine, 59 (2008), 251-265.

[43] Xiaolei Z, Xiao Y, Plaxco KW. Journal of the American Chemical Society, 131 (2009), 6944-6945.

[44] Ellington AD, Szostak JW. Nature, 346 (1990), 818-822.

[45] Tuerk C, Gold L. Science, 249 (1990), 505-510.

[46] Iqbal SS, Mayo MW, Brune JG, Bronk BV, Batt CA, Chambers JP. Biosensors and Bioelectronics, 15 (2000).

[47] Xiao Y, Plaxco KW. “Electrochemical aptamer sensors.” Function Nucleic Acids for Sensing and Other Analytical Applications; Lu Y, Li Y, Eds.; Kluwer/Springer: New York, (2009), 179-198.

[48] Rosi NL, Mirkin CA. Chemical Reviews, 105 (2004), 1547-1562.

[49] Alivisatos P. Nature Biotechnology, 22 (2004), 47-54.

[50] Jin R, Cao Y, Hao E, Metraux GS, Schatz GC, Mirkin CA. Science, 425 (2003), 487-491.

[51] Sau TK, Murphy CJ. Journal of the American Chemical Society, 126 (2004), 8648-8653.

[52] Cui Y, Wei Q, Park H, Lieber CM. Science, 293 (2003), 1289-1293.

[53] Ramgir NS, Yang Y, Zacharias M. Small, 6 (2011), 1705-1722.

[54] Patolsky F, Zheng GF, Hayden O, Lieber CM. Proceeding of the National Academy of Sciences USA, 101 (2004), 14017-14022.

[55] Stern E, Klemic JF, Routenberg DA, Wyrembak PN, Turner-Evans DB, Hamilton AD, LaVan DA, Fahmy TM, Reed MA. Nature, 445 (2007), 519-522.

[56] Zheng, GF, Patolsky F, Cui Y, Wang W, Lieber CM. Nature Biotechnology, 23 (2005), 1294-1301.

[57] Wang WU, Chen C, Lin KH, Fang Y, Lieber CM. Publications of the Nation Academy of Sciences USA, 102 (2005), 3208-3212.

[58] Sheehan PE, Whitman LJ. Nano Letters, 5 (2005), 803-807.

[59] Squires TM, Messinger RJ, Manalis SR. Nature Biotechnology, 26 (2008), 417-426.

[60] Waggoner A. Current Opinions in Chemical Biology, 10 (2006), 62-66.

[61] Levin MK, Carson JH. Differentiation, 72 (2004), 1-10.

[62] Wennmalm S, Widengren J. Frontiers in Bioscience, 3 (2011), 385-392.

[63] Li L, Song J, Li S, Fan C. Journal of Physics D: Applied Physics, 42 (2009), 203001-203012.

[64] Wang W, Chen C, Qian M, Zhao XS. Analytical Biochemistry, 373 (2008), 213-219.

[65] Dong H, Gao W, Yan F, Ji H, Huangxian J. Analytical Chemistry, 82 (2011), 5511-5517.

[66] Medintz IL, Clapp AR, Brunel FM, Tiefenbrunn T, Uyeda HT, Chang EL, Deschamps JR, Dawson PE, Mattoussi H. Nature Materials, 5 (2006), 581-589.

[67] Heid CA, Stevens J, Livak KJ, Williams PM. Genomic Research, 6 (1996), 986-994.

[68] Giljohann DA, Mirkin CA. Nature, 462 (2009), 461-464.

[69] Mirkin CA, Letsinger RL, Mucic RC, Storhoff, JJ. Nature, 382 (1996), 607-609.

[70] Nam JM, Park SJ, Mirkin CA. Journal of the American Chemical Society, 124 (2002), 3820-3821.

[71] Baptista P, Pereira E, Eaton P, Doria G, Miranda A, Gomes I, Quaresma P, Franco R. Analytical and Bioanalytical Chemistry, 391 (2008), 943-950.

[72] Sepulveda B, Angelome PC, Lechuga LM, Liz-Marzan LM. Nano Today, 4 (2009), 244-251.

[73] Anker JN, Hall WP, Lyandres O, Shah NC, Zhao J, Van Duyne RP. Nature, 7 (2008), 442-453.

[74] Waldeisen JR, Wang T, Ross BM, Lee LP. American Chemical Society Nano, 7 (2011), 5383-5389.

[75] Dahlin AB, Chen S, Jonsson MP, Gunnarsson L, Kall M, Hook F. Analytical Chemistry, 81 (2009).

[76] McFarland AD, Van Duyne RP. Nano Letters, 3 (2003), 1057–1062.

[77] Hirsch LR, Jackson JB, Lee A, Halas NJ, West J. Analytical Chemistry, 75 (2003), 2377–2381.

[78] Larsson EM, Alegret J, Kall M, Sutherland DS. Nano Letters, 7 (2007), 1256–1263.

[79] Lu Y, Liu GL, Kim J, Mejia YX, Lee LP. Nano Letters, 5 (2005), 119–124.

[80] Rindzevicius T, Alaverdyan Y, Dahlin A, Hook F, Sutherland DS, Kall M. Nano Letters, 5 (2005), 2335–2339.

[81] Zhang J, Wang L, Pan D, Song S, Boey FYC, Zhang H, Fan Chunhai. Small, 8 (2008), 1196-1200.

[82] Liu J, Lu Y. Angewandte Chemie-International Edition, 45 (2006), 90-94.

[83] Thanh NTK, Rosenzweig Z. Analytical Chemistry, 74 (2002), 1624-1630.

[84] Liao H, Hafner JH. Chemistry of Materials, 17 (2005), 4636-4641.

[85] Wang Z, Levy R, Fernig DG, Brust M. Journal of the American Chemical Society, 128 (2006), 2214-2215.

[86] Kreuzer MP, Quidant R, Badenes G, Marco MP. Biosensors and Bioelectronics, 21 (2006), 1345-1349.

[87] Kreuzer MP, Quidant R, Salvador JP, Marco MP, Badenes G. Analytical and Bioanalytical Chemistry, 391 (2008), 1813-1820.

[88] Kooyman, Rob PH. "Physics of Surface Plasmon Resonance." Handbook of Surface Plasmon Resonance; Schasfoort RMB, Tudos AJ, Eds.; Royal Society of Chemistry: Cambridge, (2008), 15-34.

[89] Kneipp K, Kneipp H, Itzkan I, Dasari RR, Feld MS. Journal of Physics: Condensed Matter, 14 (2002), 597-568.

[90] Cao YC, Jin R, Nam J-M, Thaxton CS, Mirkin CA. Journal of the American Chemical Society, 125 (2003), 14676-14677.

[91] MacBeath G, Schreiber SL. Science, 289 (2000), 1760-1763.

[92] Nie S, Emory SR. Science, 275 (1997), 1102-1106.

[93] Kneipp K, Wang Y, Kneipp H, Perelman LT, Itzkan I, Dasari R, Feld MS. Physics Review Letters, 78 (1997), 1667-1670.

[94] Gao S, Koshizaki N. Analytical and Bioanalytical Chemistry, 399 (2011), 91-101.

[95] Coto-Garcia AM, Sotelo-Gonzalez E, Fernandez-Arguelles MT, Pereiro R, Costa-Fernandez JM, Sanz-Mele A. Analytical and Bioanalytical Chemistry, 399 (2011), 29-42.

[96] Ladbury JE, Klebe G, Freire E. Nature Review: Drug Discovery, 9 (2010), 23-27.

[97] Roselin LS, Lin M-S, Lin P-H, Chang Y, Chen W-Y. Journal of Biotechnology, 5 (2010), 85-98.

[98] Indyk L, Fisher HF. Methods in Enzymology, 295 (1998), 350-364.

[99] Weber G. Journal of Physical Chemistry, 99 (1995), 1052-1059.

[100] Falconer RJ, Collins BM. Journal of Molecular Recognition, 24 (2010), 1-16.

[101] Falconer RJ, Anita P, Illian J, Collins BM. Journal of Molecular Recognition, 23 (2009), 395-413.

[102] Housden NG, Kleanthous C, Johnson ML, Holt JM, Ackers GK. Methods in Enzymology, (2011).

[103] Piepenbrink KH, Gloor BE, Armstrong KM, Baker BM. Methods in Enzymology, 466 (2009), 359-381.

[104] Liang Yi. Acta Biochemica and Biophysica Sinica.

[105] Velazquez-Campoy A, Freire E. Nature Protocols, 1 (2006), 186-191.

[106] "Products - Isothermal Titration Calorimetry." GE Healthcare: ULTRASENSITIVE CALORIMETRY FOR THE LIFE SCIENCES, (2008), accessed September 2011. <http://www.microcal.com/products/itc/itc200.asp>.

[107] Brockman JM, Nelson BP, Corn RM. Annual Review of Physical Chemistry, 51 (2000), 41-63.

[108] Lange U, Roznyatouskaya N, Mirsky V. Analytica Chimica Acta, 614 (2008), 1-26.

[109] Leonard P, Hearty S, Brennan J, Dunne L, Quinn J, Chakraborty T, O'Kennedy R. Enzyme and Microbial Technology, 32 (2003), 3-13.

[110] Bower JF, Pannifer A. Current Pharmaceutical Design, 18 (2012), 4685-4696.

[111] Otto A. Zeitschrift fuer Physik, 216 (1968), 398-410.

[112] Kretschmann E. Z Physics, 241 (1971), 313-324.

[113] GE Healthcare: Biacore. Surface plasmon resonance, Technology Note 1, 2008.

[114] Wark AW, Lee HJ, Corn RM. Analytical Chemistry, 77 (2005), 3904-3907.

[115] Cairns GF, O'Prey SM, Dawson P. Review of Scientific Instruments, 71 (2000), 4213-4222.

[116] Scarano S, Mascini M, Turner APF, Minunni M. Biosensors & Bioelectronics, 25 (2010), 957-966.

[117] Situ C, Buijs J, Mooney MH, Elliot CT. Trends in Analytical Chemistry, 29 (2010), 1305-1315.

[118] Chinowsky TM, Mactutis T, Fu E, Yager P. Smart Medical and Biomedical Sensor Technology, Proceedings of SPIE, (2004), 5261.

[119] Kodak. Application Note: CCD Image Sensor Noise Sources. Image Sensor Solutions, (2005).

[120] Winspall computer program developed by the Wolfgang Knoll group in Mainz, Germany.

[121] Stenberg E, Persson B, Roos H, Llrbanlczky C. Journal of Colloidal Interface Science, 143 (1991), 513-526.

[122] Tudos AJ, Schasfoort RBM. "Introduction to Surface Plasmon Resonance." Handbook of Surface Plasmon Resonance. Eds. Schasfoort RBM, Tudos AJ. Royal Society of Chemistry: Cambridge, (2008), 1-14.

[123] Myszka DG. Analytical Biochemistry, 329 (2004), 316-323.

[124] Karlsson R, Roos H, Lars F, Persson B. Methods in Enzymology, 6 (1994), 99-110.

[125] Scarano S, Mascini M, Turner APF, Minunni M. Biosensors & Bioelectronics, 25 (2010), 957-966.

[126] Bower JF, Pannifer A. Current Pharmaceutical Design, 18 (2012), 4685-4696.

[127] Wang S, Shan X, Patel U, Huang X, Lu J, Li J, Tao NJ. Publication of the National Academy of Sciences, 107 (2010), 16028-16032.

[128] Lee JR, Magee DM, Gaster RS, LaBaer J, Wang SX. Expert Review of Proteomics, 10 (2013), 65-75.

[129] Geschwindner S, Carlsson JF, Knecht W. Sensors, 12 (2012), 4311.

[130] Myszka DG. Current Opinion in Biotechnology. 1997, 8, 50-57.

[131] Doyle ML, Myszka DG, Chaiken IM. Journal of Molecular Recognition, 9 (1996), 65-74.

[132] Hensley P. Current Opinion in Biotechnology, 4 (1996), 367-373.

[133] de Crescenzo G, Boucher C, Durocher Y, Jolicoeur M. Cellular and Molecular Bioengineering,1 (2008), 204-210.

[134] Tamada K, Hara M, Sasabe H, Knoll W. Langmuir, 13 (1997), 1558–1566.

[135] Strong L, Whitesides GM. Langmuir, 4 (1988), 546–558.

[136] Sua X, Teh FH, Aunga K, Zonga Y, Gao Z. Biosensors and Bioelectronics, 23 (2008), 1715–1720.

[137] Morton TA, Myszka DG, Chaiken IM. Analytical Biochemistry, 227 (1995), 176-185.

[138] Myszka DG, Morton TA, Doyle ML, Chaiken IM. Biophysical Chemistry, 64 (1997), 127-137.

[139] Wang S, Boussaad S, Tao NJ. "Surface Plasmon Resonance Spectroscopy." Biomolecular Films. E.d. James F Rusling. Marcel Dekker, Inc.: New York (2003) 213-251.

[140] Biosensing USA. <http://www.biosensingusa.com/Application102.html> accessed in June 2013.

[141] Shalabney A, Abdulhalim I. Laser & Photonics Review, 5 (2011), 571-606.

[142] Campbell CT, Kim G. Biomaterials, 28 (2007), 2380-2392.

[143] Khalifa MB, Choulier L, Lortat-Jacob H, Altschuh D, Vernet T. Analytical Biochemistry, 293 (2001), 194-203.

[144] Glaser RW. Analytical Biochemistry, 213 (1993), 152-161.

[145] Karlsson R, Roos H, Fägerstam L, Persson B. Methods in Enzymology, 6 (1994), 99-110.

[146] Christensen LLH. Analytical Biochemistry, 249 (1997), 153-164.

[147] Goldstein B, Coombs D, He X, Pineda AR, Wofsy C. Journal of Molecular Recognition, 12 (1999), 293-299.

[148] Schuck P. Biophysical Journal, 70 (1996), 1230-1249.

[149] Myzka DG, He X, Dembo M, Morton TA, Goldstein B. Biophysical Journal, 75 (1998), 583-594.

[150] Information found on companies' websites or by phone or email solicitation in June 2013.

[151] COMSOL Model #315. <http://www.comsol.com/showroom/gallery/315/> accessed in June 2013.

[152] Lu J, Wang W, Wang S, Shan X, Li J, Tao NJ. Analytical Chemistry, 84 (2012), 327-333.

[153] Kotz R, Kolb DM, Sass JK. Surface Science, 69 (1977), 359-364.

[154] Wang S, Boussaad S, Wong S, Tao NJ. Analytical Chemistry, 72 (2010), 4003-4008.

[155] Foley KJ, Shan X, Tao NJ. Analytical Chemistry, 80 (2008), 5146-5151.

[156] Wang S, Huang XP, Shan X, Foley K, Tao NJ. Analytical Chemistry, 82 (2010), 935-941.

[157] Huang XP, Wang S, Shan X, Chang X, Tao NJ. Journal of Electroanalytical Chemistry, 69 (2010), 37-41.

[158] Shan X, Huang X, Foley K, Zhang P, Chen K, Wang S, Tao NJ. Analytical Chemistry, 82 (2010), 234-240.

[159] Shan X, Wang S, Tao NJ. Applied Physics Letters, 97 (2010), 223703:1-3.

[160] Krishnamoorthy G, Carlen ET, van den Berg A, Schasfoort RBM. Sensors and Actuators B: Chemical, 148 (2010), 511-521.

[161] DrugBank 3.0: A comprehensive resource for 'omics' research on drugs. Knox C, Law V, Jewison T, Liu P, Ly S, Frolkis A, Pon A, Banco K, Mak C, Neveu V, Djoumbou Y, Eisner R, Guo AC, Wishart DS. Nucleic Acids Research, 39 (2011), D1035-41.

[162] Haake, HM, Schutz A, Gauglitz G. Fresenius's Journal of Analytical Chemistry, 366 (2000), 576-585.

[163] Morgan CL, Newman DJ, Price CP. Clinical Chemistry, 42 (1996), 193-209.

[164] McNeil CJ, Athey D, Rennerberg R. In: Scheller FM, Schubert F, Fedrowitz J, Eds.; Frontiers in Biosensorics. Practical Applications; Birkhäuser: Basel, Switzerland, (1997) 17-25.

[165] Skladal P. Electroanalysis, 9 (1997), 737-745.

[166] Ray S, Mehta G, Srivastava S. Proteomics, 10 (2010), 731-748.

[167] Espina V, Woodhouse EC, Wulfkuhle J, Asmussen HD, Petricoin EF III, Loitta LA. Journal of Immunological Methods, 290 (2004), 121-133.

[168] Wassaf D, Kuanga G, Kopacz K, Wu Q-L, Nguyen Q, Toews M, Cosic J, Jacques J, Wiltshire S, Lambert J, Pazmanya CC, Hogan S, Ladner RC, Nixon AE, Sexton DJ. Analytical Biochemistry, 351 (2006), 241-253.

[169] Shan XN, Patel U, Wang SP, Iglesias R, Tao NJ. Science, 327 (2010) 1363−1366.

[170] Wang W, Foley K, Shan X, Wang SP, Eaton S, Nagaraj VJ, Wiktor P, Patel U, Tao NJ. Nature Chemistry, 3 (2011), 249−255.

[171] Shan X, Wang S, Wang W, Tao NJ. Analytical Chemistry, 83 (2011), 7394−7399.

[172] Lu J, Wang W, Wang SP, Shan XN, Li J, Tao NJ. Analytical Chemistry, 84 (2012), 327-333.

[173] Cohen P. Nature Cell Biology, 4 (2002), E127-E130.

[174] Gutz, I. G. R. (2012). Curtipot program, Version 3.6.1, pH and Acid-Base titration curves: Analysis and Simulation [Online].

[175] MacGriff C, Wang S, Wiktor P, Wang W, Shan X, Tao NJ. Analytical Chemistry, 85 (2013), 6682-6687.

[176] MacGriff C, Wang S, Tao NJ. Review of Scientific Instruments, 84 (2013), 106110-3.

APPENDIX A

DERIVATION OF THE SURFACE PLASMON DISPERSION RELATION

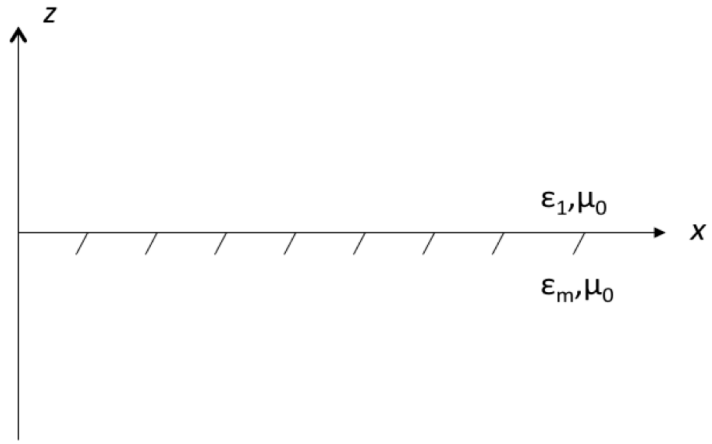

Figure A1. Interface of two media and their respective constitutive parameters.

z<0

$$\boldsymbol{E_1} = (\hat{a}_x E_{x1} + \hat{a}_z E_{z1}) e^{-j(k_{x1}x - k_{z1}z)} \tag{1a}$$

$$\boldsymbol{H_1} = \hat{a}_y H_{y1} e^{-j(k_{x1}x - k_{z1}z)} \tag{1b}$$

z>0

$$\boldsymbol{E_2} = (\hat{a}_x E_{x2} + \hat{a}_z E_{z2}) e^{-j(k_{x2}x + k_{z2}z)} \tag{2a}$$

$$\boldsymbol{H_2} = \hat{a}_y H_{y2} e^{-j(k_{x2}x + k_{z2}z)} \tag{2b}$$

A.1 Time-Harmonic Electromagnetic Fields

The propagation of electromagnetic radiation in the two semi-infinite nonmagnetic media in Figure A1 can be described by Maxwell's equations. The index i describes the media: $i = 1$ at $z < 0$ and $i = 2$ at $z > 0$.

$$\nabla \times \boldsymbol{E_i} = -j\omega\mu \boldsymbol{H_i} \tag{3}$$

$$\nabla \times \boldsymbol{H_i} = j\omega\varepsilon_i \boldsymbol{E_i} \tag{4}$$

$$\nabla \cdot \boldsymbol{D_i} = \boldsymbol{q}_{evi} \tag{5}$$

$$\nabla \cdot \boldsymbol{B_i} = \boldsymbol{q}_{mvi} \tag{6}$$

$\boldsymbol{E}$ = electric field intensity (V/m)
$\boldsymbol{H}$ = magnetic field intensity (A/m)
$\boldsymbol{D}$ = electric flux density (C/m^2)
$\boldsymbol{B}$ = magnetic flux density (W/m^2)
$\boldsymbol{J}_i$ = impressed (source) electric current density (A/m^2)
$\boldsymbol{J}_c$ = conduction electric current density (A/m^2)
$\boldsymbol{J}_d$ = displacement electric current density (V/m^2)
$\boldsymbol{M}_i$ = impressed (source) magnetic current density (V/m^2)
$\boldsymbol{M}_d$ = displacement magnetic current density (V/m^2)
$\boldsymbol{q}_{ev}$ = electric charge density (C/m^3)
$\boldsymbol{q}_{mv}$ = magnetic charge density (W/m^3)
μ_0 = 4π x 10^{-7} (H/m)
ε_0 = 8.854 x 10^{-12} (F/m)
σ_s = static field conductivity
σ_a = alternating field conductivity
σ_e = sigma s + sigma e equivalent conductivity

$$e^{j\omega t}\ time\ convention$$

Asumption1: source free regions $\boldsymbol{q}_{ev} = 0$ and $\boldsymbol{M}_i = \boldsymbol{q}_{mv} = 0$ and lossless ($\sigma_s = 0$). Non ferrous mediums $\mu_0\mu_1 = \mu_0\mu_2 = \mu_0$

$$\nabla\times\boldsymbol{E} = -j\omega\mu\boldsymbol{H}$$

$$\nabla\times\boldsymbol{E_1} = \begin{vmatrix} \hat{a}_x & \hat{a}_y & \hat{a}_z \\ \partial/\partial x & \partial/\partial y & \partial/\partial z \\ E_{x1}e^{e^{-j(k_{x1}x-k_{z1}z)}} & 0 & E_{z1}e^{e^{-j(k_{x1}x-k_{z1}z)}} \end{vmatrix}$$

$$= \hat{a}_x\left[\frac{\partial}{\partial y}\left(E_{z1}e^{-j(k_{x1}x-k_{z1}z)}\right)\right] - \hat{a}_y\left[\frac{\partial}{\partial x}\left(E_{z1}e^{-j(k_{x1}x-k_{z1}z)}\right) - \frac{\partial}{\partial z}\left(E_{x1}e^{-j(k_{x1}x-k_{z1}z)}\right)\right]$$

$$- \hat{a}_z\left[\frac{\partial}{\partial y}\left(E_{x1}e^{-j(k_{x1}x-k_{z1}z)}\right)\right]$$

$$= \hat{a}_x \left[e^{-j(k_{x1}x - k_{z1}z)} \frac{\partial E_{z1}}{\partial y} \right] - \hat{a}_y \left[e^{-j(k_{x1}x - k_{z1}z)} \left(\frac{\partial E_{z1}}{\partial x} - jk_{x1}E_{z1} - \frac{\partial E_{x1}}{\partial z} - jk_{z1}E_{x1} \right) \right]$$

$$- \hat{a}_z \left[e^{-j(k_{x1}x - k_{z1}z)} \frac{\partial E_{x1}}{\partial y} \right]$$

The value of E_n represents the amplitude of the electric field wave traveling in the $\hat{n}$ direction, and is constant such that $\frac{\partial E_z}{\partial y} = \frac{\partial E_z}{\partial x} = 0$, $\frac{\partial H_{y1}}{\partial t} = 0$ etc.

$$\nabla \times \boldsymbol{E_1} = -\hat{a}_y \left[e^{-j(k_{x1}x - k_{z1}z)} (-jk_{x1}E_{z1} - jk_{z1}E_{x1}) \right]$$

$$-j\omega\mu_0 \boldsymbol{H_1} = -\hat{a}_y \left[j\omega\mu_0 H_{y1} e^{-j(k_{x1}x - k_{z1}z)} \right]$$

Applying (3) to (1) and (2):

$$-jk_{x1}E_{z1} - jk_{z1}E_{x1} = j\omega\mu_0 H_{y1} \tag{7a}$$

$$-jk_{x2}E_{z2} + jk_{z2}E_{x2} = j\omega\mu_0 H_{y2} \tag{7b}$$

$$\nabla \times \boldsymbol{\mathcal{H}} = j\omega\varepsilon \boldsymbol{E}$$

$$\nabla \times \boldsymbol{H_1} = \begin{vmatrix} \hat{a}_x & \hat{a}_y & \hat{a}_z \\ \partial/\partial x & \partial/\partial y & \partial/\partial z \\ 0 & H_{y1} e^{-j(k_{x1}x - k_{z1}z)} & 0 \end{vmatrix}$$

$$= -\hat{a}_x \left[\frac{\partial}{\partial z} \left(H_{y1} e^{-j(k_{x1}x - k_{z1}z)} \right) \right] + \hat{a}_z \left[\frac{\partial}{\partial x} \left(H_{y1} e^{-j(k_{x1}x - k_{z1}z)} \right) \right]$$

$$= -\hat{a}_x \left[e^{-j(k_{x1}x - k_{z1}z)} \left(\frac{\partial H_{y1}}{\partial z} + jk_{z1}H_{y1} \right) \right] + \hat{a}_z \left[e^{-j(k_{x1}x - k_{z1}z)} \left(\frac{\partial H_{y1}}{\partial x} - jk_{x1}H_{y1} \right) \right]$$

$$= -\hat{a}_x \left[jk_{z1}H_{y1} e^{-j(k_{x1}x - k_{z1}z)} \right] - \hat{a}_z \left[jk_{x1}H_{y1} e^{-j(k_{x1}x - k_{z1}z)} \right]$$

$$j\omega\varepsilon_0\varepsilon_1\boldsymbol{E_1} = j\omega\varepsilon_0\varepsilon_1(\hat{a}_x E_{x1} + \hat{a}_z E_{z1})e^{-j(k_{x1}x - k_{z1}z)}$$

$$= \hat{a}_x\left[j\omega\varepsilon_0\varepsilon_1 E_{x1}e^{-j(k_{x1}x-k_{z1}z)}\right] + \hat{a}_z\left[j\omega\varepsilon_0\varepsilon_1 E_{z1}e^{-j(k_{x1}x-k_{z1}z)}\right]$$

$$\nabla\times\boldsymbol{H_1} = j\omega\varepsilon_0\varepsilon_1\boldsymbol{E_1} = -\hat{a}_x\left[jk_{z1}H_{y1}e^{-j(k_{x1}x-k_{z1}z)}\right] - \hat{a}_z\left[jk_{x1}H_{y1}e^{-j(k_{x1}x-k_{z1}z)}\right]$$

$$= \hat{a}_x\left[j\omega\varepsilon_0\varepsilon_1 E_{x1}e^{-j(k_{x1}x-k_{z1}z)}\right] + \hat{a}_z\left[j\omega\varepsilon_0\varepsilon_1 E_{z1}e^{-j(k_{x1}x-k_{z1}z)}\right]$$

From applying (4) to (1) and (2):

$$-jk_{z1}H_{y1} = j\omega\varepsilon_0\varepsilon_1 E_{x1} \tag{8a}$$

$$-jk_{x1}H_{y1} = j\omega\varepsilon_0\varepsilon_1 E_{z1} \tag{8b}$$

$$jk_{z2}H_{y2} = j\omega\varepsilon_0\varepsilon_2 E_{x2} \tag{8c}$$

$$-jk_{z2}H_{y2} = j\omega\varepsilon_0\varepsilon_2 E_{x2} \tag{8d}$$

Boundary Conditions; Finite Conductivity Media

$$\hat{n}\times(\boldsymbol{\mathcal{E}}_2 - \boldsymbol{\mathcal{E}}_1) = 0 \tag{9}$$

$$\hat{n}\times(\boldsymbol{\mathcal{H}}_2 - \boldsymbol{\mathcal{H}}_1) = 0 \tag{10}$$

$$E_{x1} = E_{x2} \tag{11a}$$

$$H_{y1} = H_{y2} \tag{11b}$$

$$k_{1x} = k_{2x} \tag{11c}$$

Using equations (11a-c), equations (7a) and (7b) can be rewritten as:

$$-k_x E_{z1} - k_{z1}E_x = \omega\mu_0 H_y \tag{12a}$$

$$-k_x E_{z2} + k_{z2}E_x = \omega\mu_0 H_y \tag{12b}$$

Using (11a-c), equations (8a-d) can be rewritten as:

$$-\frac{k_{z1}H_y}{\omega\varepsilon_0\varepsilon_1} = E_x \tag{13a}$$

$$-\frac{k_x H_y}{\omega\varepsilon_0\varepsilon_1} = E_{z1} \tag{13b}$$

$$\frac{jk_{z2}H_y}{\omega\varepsilon_0\varepsilon_2} = E_x \tag{13c}$$

$$-\frac{jk_x H_y}{\omega\varepsilon_0\varepsilon_2} = E_{z2} \tag{13d}$$

The dispersion relation for surface plasmons formed at the interface between media 1 and 2 is found from (13a) and (13c).

$$-\frac{k_{z1}}{\varepsilon_1} = \frac{k_{z2}}{\varepsilon_2} \tag{14}$$

An expression for the wave vector in medium 1 is found from (13a,b) and (12b)

$$\frac{k_x^2}{\varepsilon_1} + \frac{k_{z1}^2}{\varepsilon_1} = \frac{\omega^2}{c^2} \tag{15a}$$

Similarly for medium 2: combining (13c,d) with (12a)

$$\frac{k_x^2}{\varepsilon_2} + \frac{k_{z2}^2}{\varepsilon_2} = \frac{\omega^2}{c^2} \tag{15b}$$

Plugging the dispersion relation into one of the wavevector equations and simultaneously solving for k_x gives the surface plasmon propagation vector along the interface.

$$k_x = \frac{\omega}{c}\sqrt{\frac{\varepsilon_1\varepsilon_2}{\varepsilon_1 + \varepsilon_2}} \tag{16}$$

Additionally,

$$k_{zi} = \frac{\omega}{c}\frac{\varepsilon_i}{\sqrt{\varepsilon_1 + \varepsilon_2}} \tag{17}$$

Assumption2: ω and ε_2 are real, $\varepsilon_1 = \varepsilon_1^{'} + j\varepsilon_1^{''}$

Equation (16) becomes

$$k_x = \frac{\omega}{c}\sqrt{\frac{\left(\varepsilon_1^{'} + j\varepsilon_1^{''}\right)\varepsilon_2}{\left(\varepsilon_1^{'} + j\varepsilon_1^{''} + \varepsilon_2\right)}} = \frac{\omega}{c}\sqrt{\frac{\left(\varepsilon_1^{'}\varepsilon_2 + j\varepsilon_1^{''}\varepsilon_2\right)}{\left(\varepsilon_1^{'} + \varepsilon_2 + j\varepsilon_1^{''}\right)}}\sqrt{\frac{\varepsilon_1^{'} + \varepsilon_2 - j\varepsilon_1^{''}}{\varepsilon_1^{'} + \varepsilon_2 - j\varepsilon_1^{''}}}$$

$$= \frac{\omega}{c}\sqrt{\frac{\varepsilon_1^{'}\varepsilon_2\left(\varepsilon_1^{'} + \varepsilon_2\right) + \varepsilon_1^{''2}\varepsilon_2 + j\varepsilon_1^{''}\varepsilon_2^2}{\left(\varepsilon_1^{'} + \varepsilon_2\right)^2 + \varepsilon_1^{''2}}} \tag{18}$$

k_x is complex ($k_x = k_x^{'} + jk_x^{''}$) which suggests that equation (18) be decomposed into real and complex parts.

$$k_x^2 = k_x^{'2} - k_x^{''2} + j2k_x^{'}k_x^{''} = \frac{\omega^2}{c^2}\frac{\varepsilon_1^{'}\varepsilon_2\left(\varepsilon_1^{'} + \varepsilon_2\right) + \varepsilon_1^{''2}\varepsilon_2 + j\varepsilon_1^{''}\varepsilon_2^2}{\left(\varepsilon_1^{'} + \varepsilon_2\right)^2 + \varepsilon_1^{''2}}$$

Real part:

$$k_x^{'2} - k_x^{''2} = \frac{\omega^2}{c^2}\frac{\varepsilon_1^{'}\varepsilon_2\left(\varepsilon_1^{'} + \varepsilon_2\right) + \varepsilon_1^{''2}\varepsilon_2}{\left(\varepsilon_1^{'} + \varepsilon_2\right)^2 + \varepsilon_1^{''2}} \tag{19a}$$

Imaginary part:

$$k_x^{''} = \frac{1}{2k_x^{'}}\frac{\omega^2}{c^2}\frac{\varepsilon_1^{''}\varepsilon_2^2}{\left(\varepsilon_1^{'} + \varepsilon_2\right)^2 + \varepsilon_1^{''2}} \tag{19b}$$

Plugging (19b) into (19a) and solving for $k_x^{'}$

$$k_x^{'2} = \frac{1}{2}\frac{\omega^2}{c^2}\left[\frac{\varepsilon_1^{'}\varepsilon_2\left(\varepsilon_1^{'} + \varepsilon_2\right) + \varepsilon_1^{''2}\varepsilon_2 \pm \sqrt{\left[\varepsilon_1^{'}\varepsilon_2\left(\varepsilon_1^{'} + \varepsilon_2\right) + \varepsilon_1^{''2}\varepsilon_2\right]^2 + \varepsilon_1^{''2}\varepsilon_2^4}}{\left(\varepsilon_1^{'} + \varepsilon_2\right)^2 + \varepsilon_1^{''2}}\right]$$

For Au: $\varepsilon_1^{''} < \left|\varepsilon_1^{'}\right|$, for non trivial answers, the real part of the of the x-component of the surface plasmon wave vector

$$k_x^{'} = \frac{\omega}{c}\sqrt{\frac{\varepsilon_1^{'}\varepsilon_2}{\varepsilon_1^{'} + \varepsilon_2}} \tag{20}$$

Plug (20) back into (19b) for the imaginary part

$$k_x^{''} = \frac{\omega}{c}\frac{(\varepsilon_1+\varepsilon_2)^{1/2}}{2(\varepsilon_1\varepsilon_2)^{1/2}}\frac{\varepsilon_1^{''}\varepsilon_2^2}{\left(\varepsilon_1^{'}+\varepsilon_2\right)^2+\varepsilon_1^{''2}} \tag{21}$$